



## Microtexture characterization of duplex stainless steel after hot working

Clara Herrera, Dirk Ponge, Dierk Raabe

*The 15th International Conference on the Texture of Materials (ICOTOM)  
June 1-6, 2008*



➤ **Introduction**

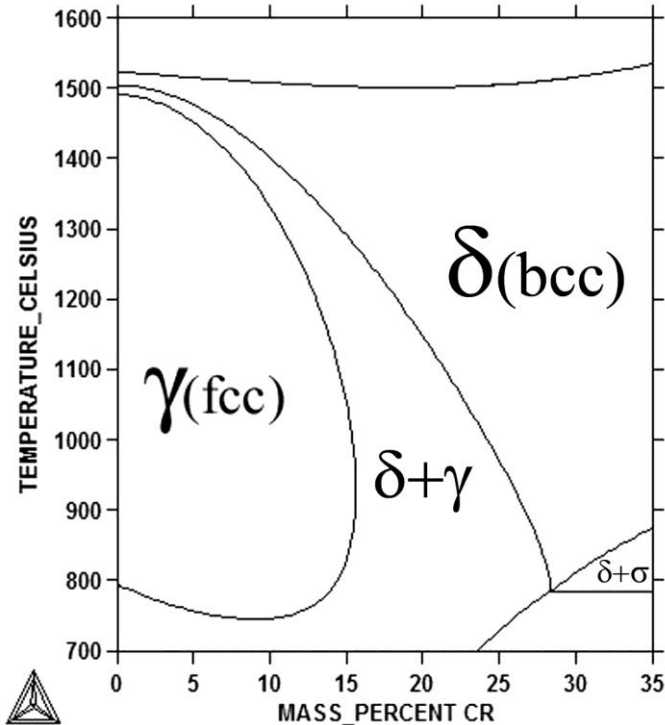
➤ **Experimental procedure**

➤ **Results**

➤ **Summary**

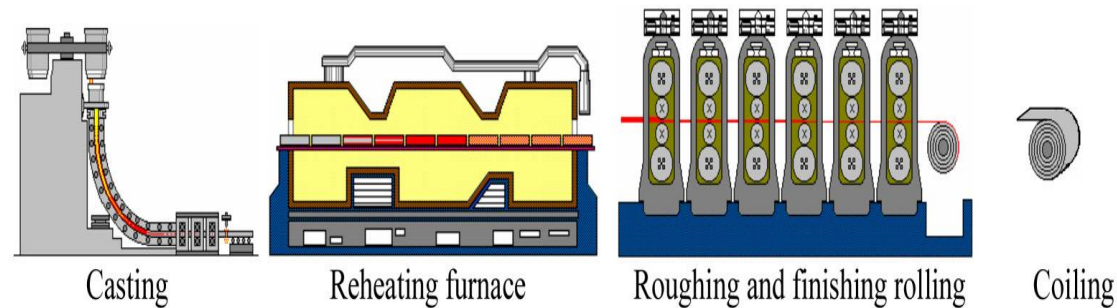
# Introduction

## Duplex stainless steels



**Fe-Cr-3.7%Ni-0.1%Mo**

### Standard industrial hot rolling schedule

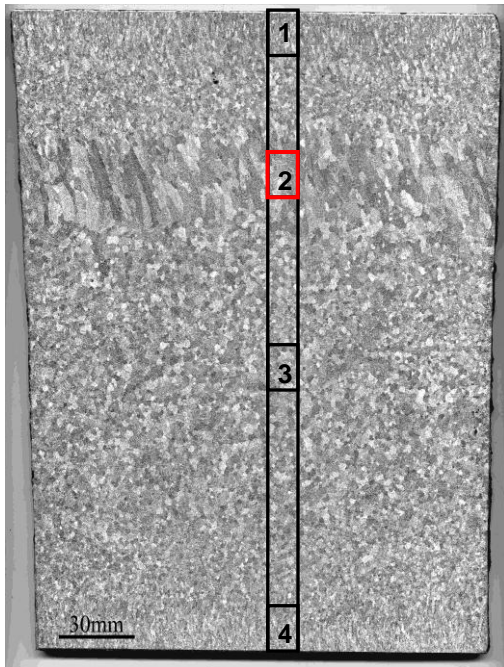


- ❖ Precipitation of a series of detrimental intermetallic phases, such as  $\sigma$ -phase.
- ❖ Low hot ductility and crack formation during hot rolling.

# Experimental procedure

## Composition (mass%)

	C	Cr	Ni	Mo	Mn	S	Si	P	Ti	N	Cu	Nb
<b>1.4362</b>	0.024	22.32	3.65	0.14	1.39	0.001	0.22	0.23	0.012	0.108	0.41	0.01



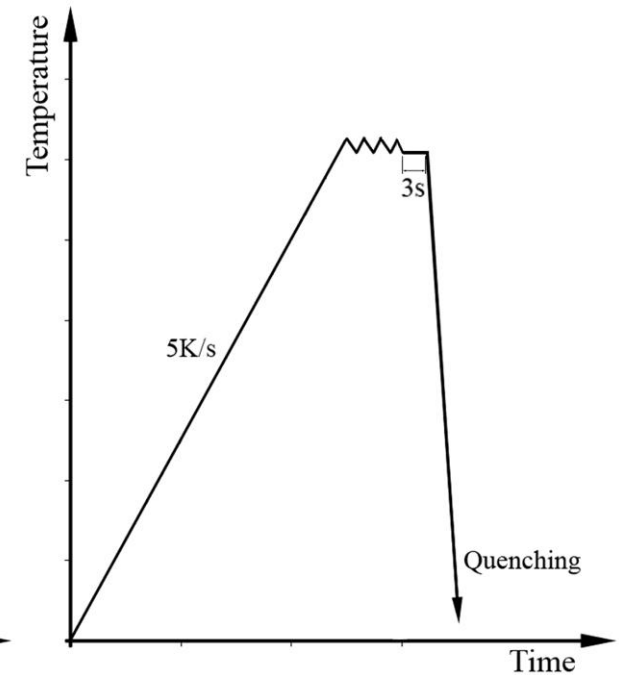
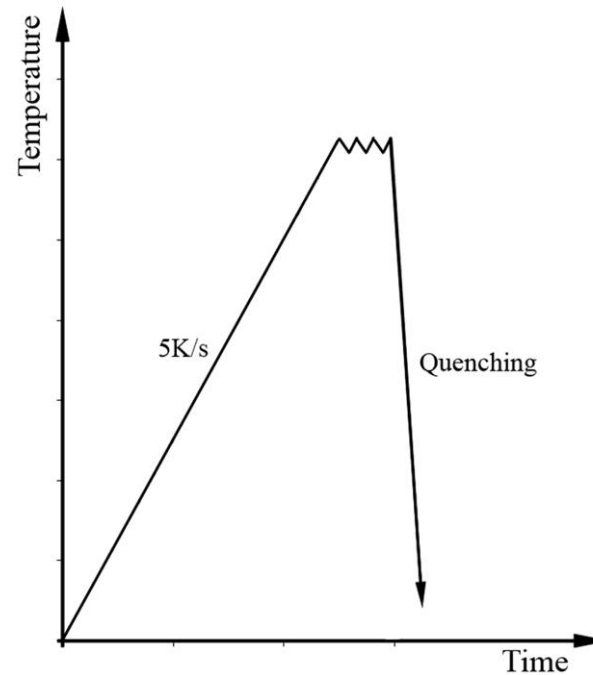
ND

TD

Casting Direction

## Uniaxial hot compression test - Dilatometer tests

$$900^{\circ}\text{C} < T < 1250^{\circ}\text{C}, \quad \varepsilon = 0.3, \quad \dot{\varepsilon} = 1\text{s}^{-1}$$



## Characterization techniques

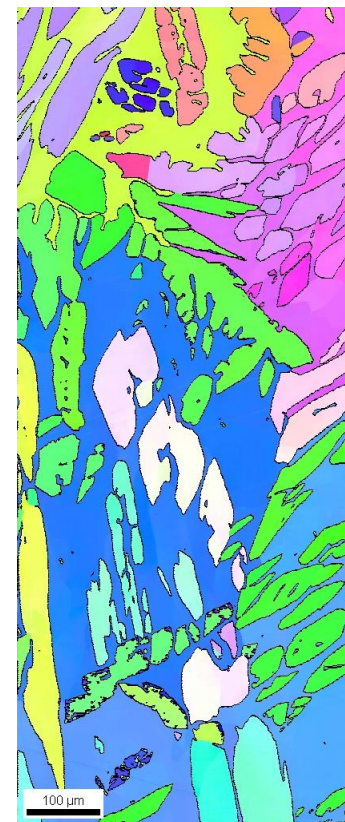
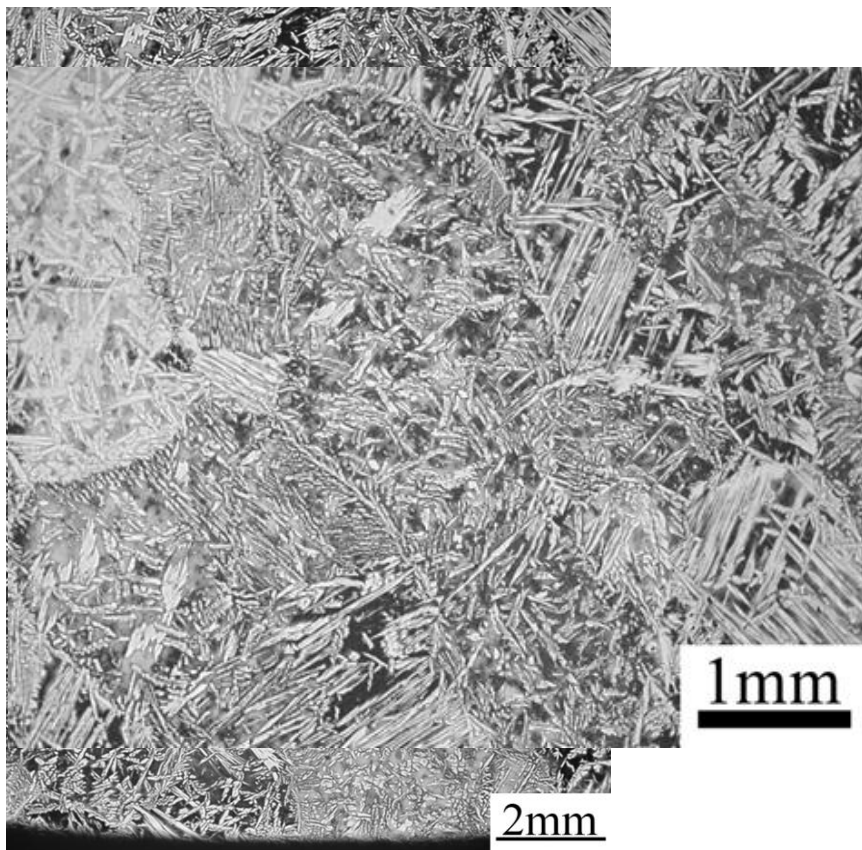
- Optical microscopy
- Microtexture measurement  $\Rightarrow$  Electron backscattering diffraction-EBSD



# Results – Initial characterization

## As cast microstructure Columnar region

Volume fraction of austenite, % =  $49,5 \pm 2,7$

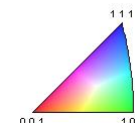
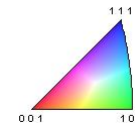


Color Coded Map Type: Phase

Phase	Total Fraction	Partition Fraction
Iron - Alpha	0.507	0.507
Iron - Gamma	0.493	0.493

Iron - Alpha

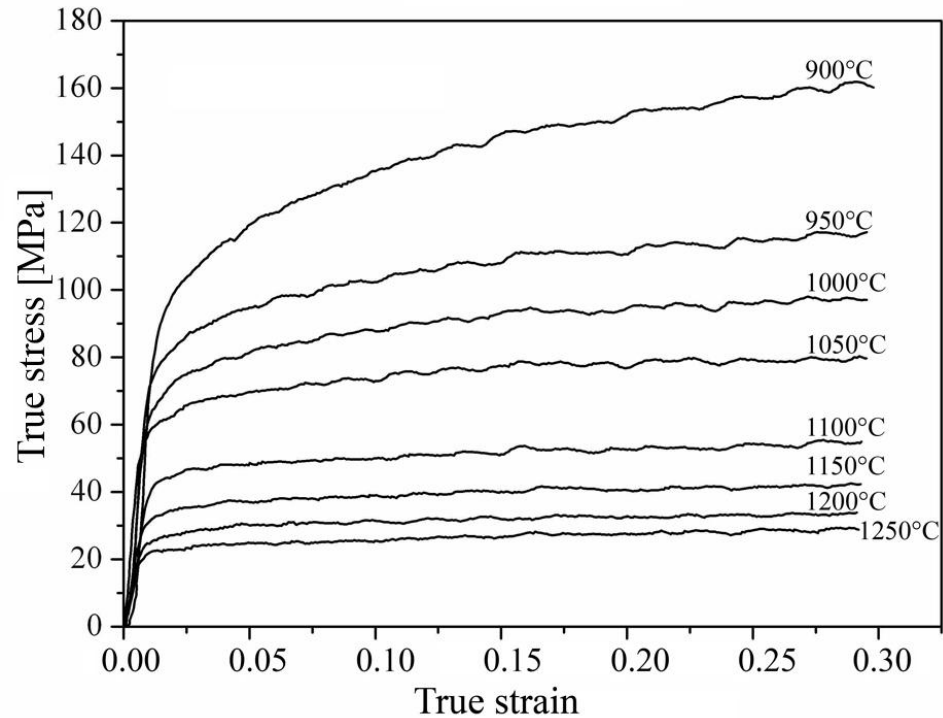
Iron - Gamma



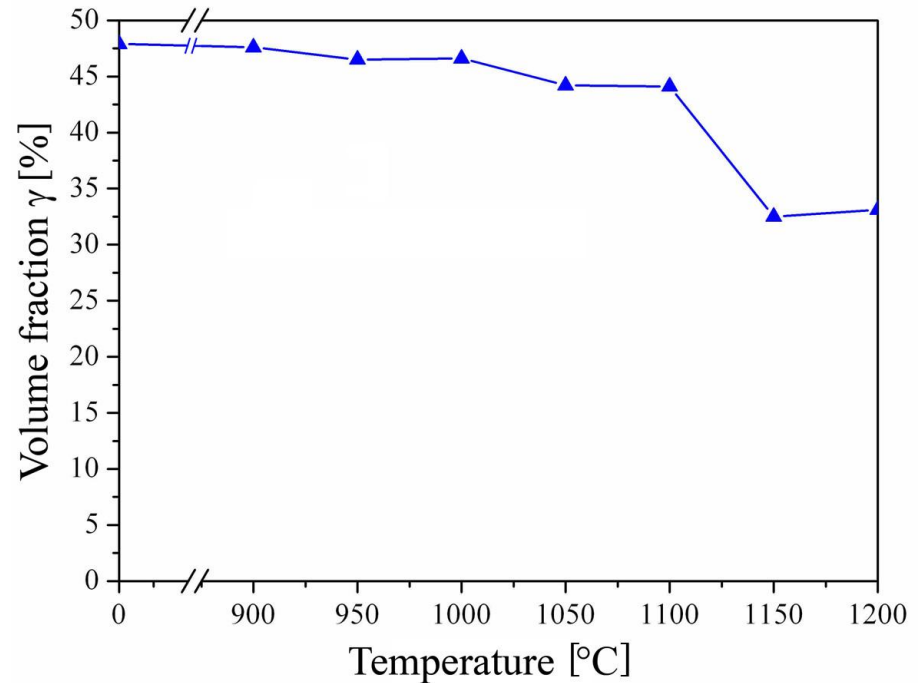
# Results – Hot deformation

## Mechanical behaviour

$$900^{\circ}\text{C} < T < 1250^{\circ}\text{C}, \quad \varepsilon = 0.3, \quad \dot{\varepsilon} = 1\text{s}^{-1}$$



*Flow curves*

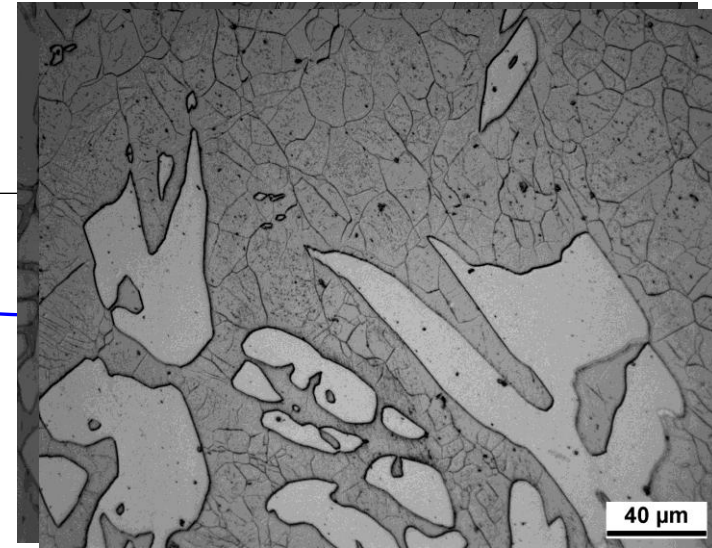
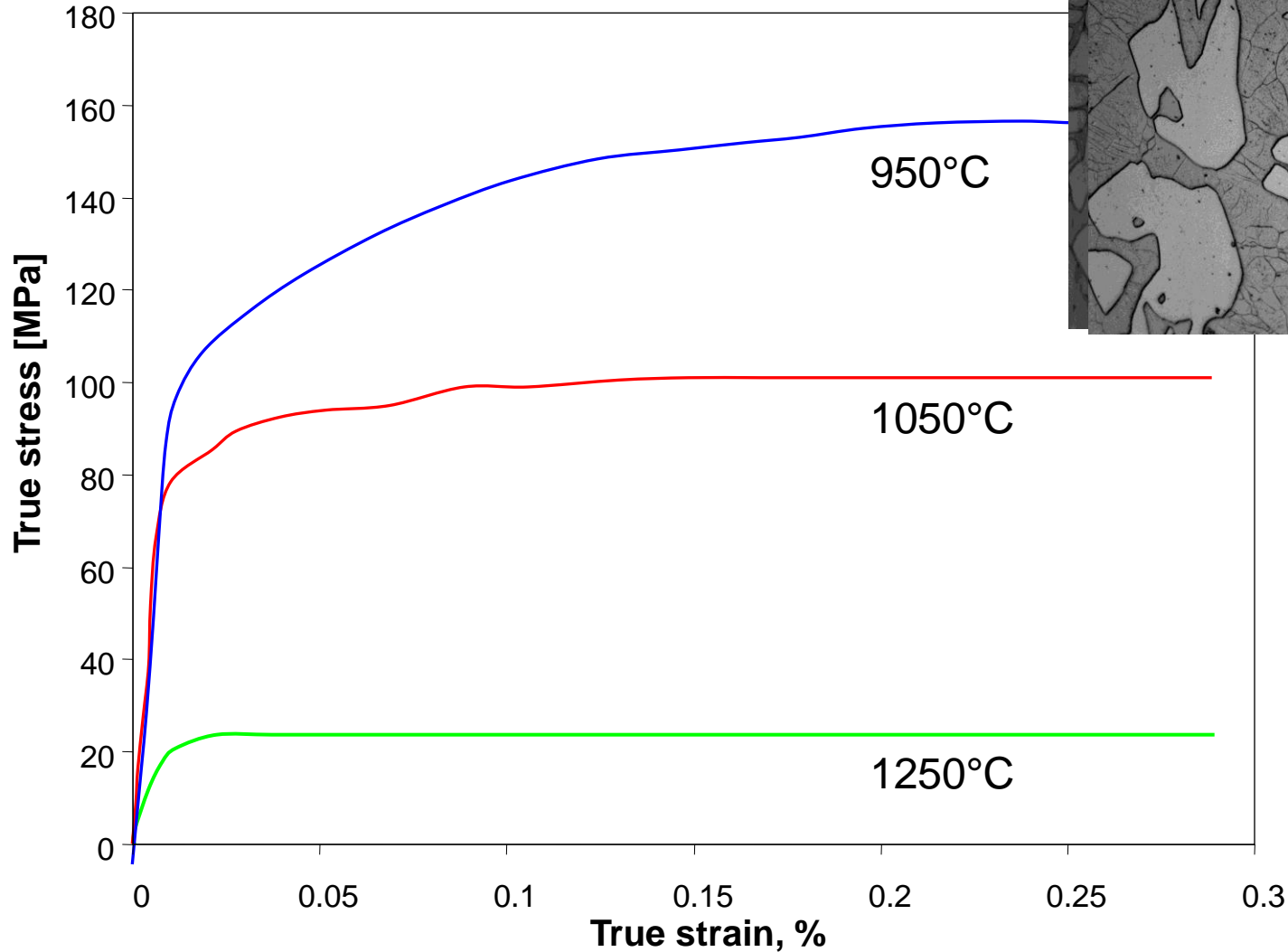


*Dependence of the volume fraction of austenite on deformation temperature*

# Results – Hot deformation

## Microstructure

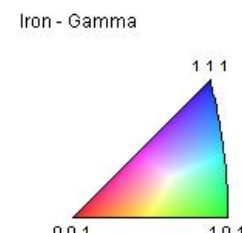
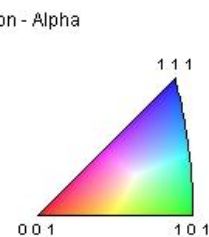
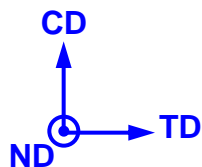
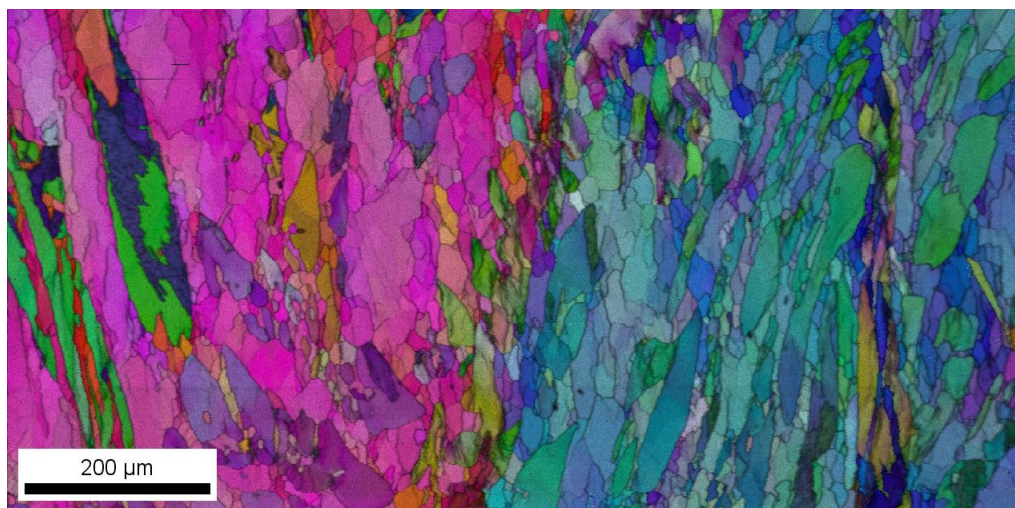
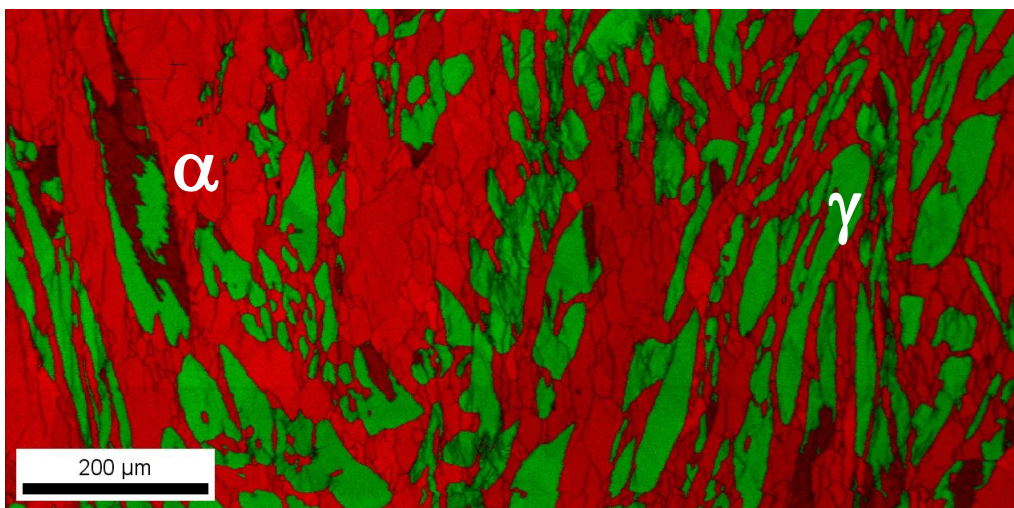
$$\varepsilon = 0.3, \quad \dot{\varepsilon} = 1s^{-1}$$



# Results – Hot deformation

## Microstructure - EBSD

$$T = 1150^{\circ}\text{C}, \quad \varepsilon = 0.3, \quad \dot{\varepsilon} = 1\text{s}^{-1}$$

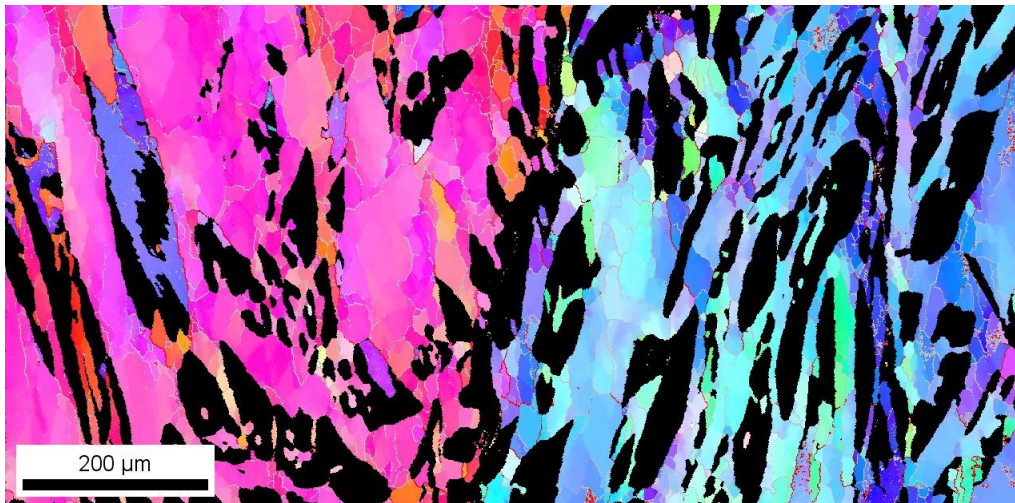




# Results – Hot deformation

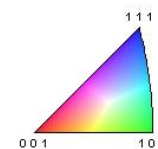
## Microstructure Ferrite

$$T = 1150^{\circ}\text{C}, \quad \varepsilon = 0.3, \quad \dot{\varepsilon} = 1\text{s}^{-1}$$



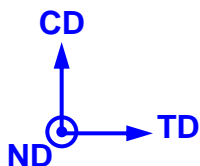
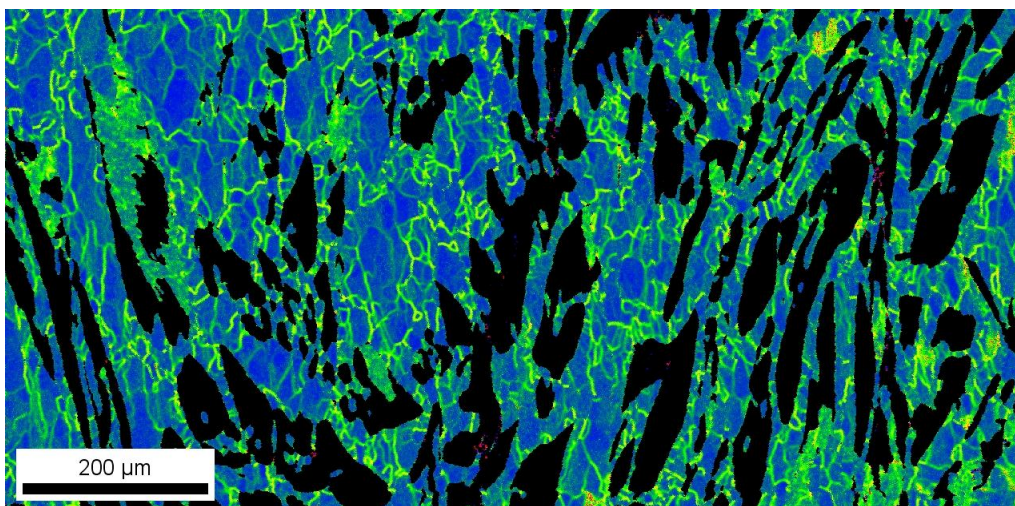
Color Coded Map Type: Inverse Pole Figure [001]

Iron - Alpha



Boundaries: Rotation Angle

	Min	Max	Fraction	Number	Length
—	2°	14.9°	0.809	54849	3.17 cm
—	15°	180°	0.189	12835	7.41 mm



Color Coded Map Type: Kernel Average Misorientation

	Min	Max	Total Fraction	Partition Fraction
—	0	5	0.661	1.000

Boundaries: <none>

# Results – Hot deformation

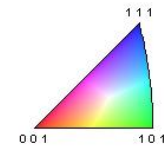
## Microstructure Austenite

$$T = 1150^{\circ}\text{C}, \quad \varepsilon = 0.3, \quad \dot{\varepsilon} = 1\text{s}^{-1}$$



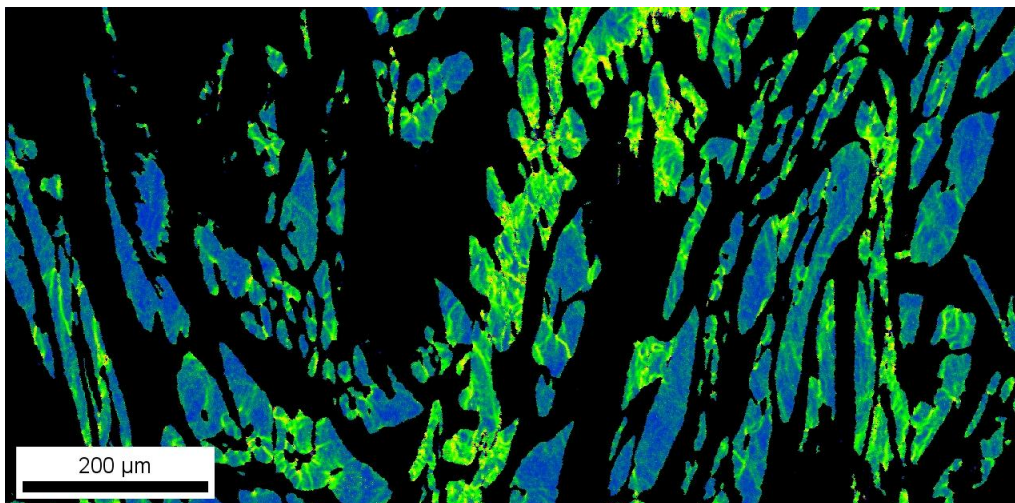
Color Coded Map Type: Inverse Pole Figure [001]

Iron - Gamma



Boundaries: Rotation Angle

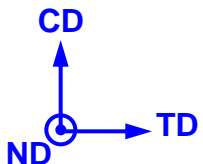
	Min	Max	Fraction	Number	Length
—	2°	14.9°	0.902	20494	1.18 cm
—	15°	180°	0.097	2204	1.27 mm



Color Coded Map Type: Kernel Average Misorientation

	Min	Max	Total Fraction	Partition Fraction
—	0	5	0.339	1.000

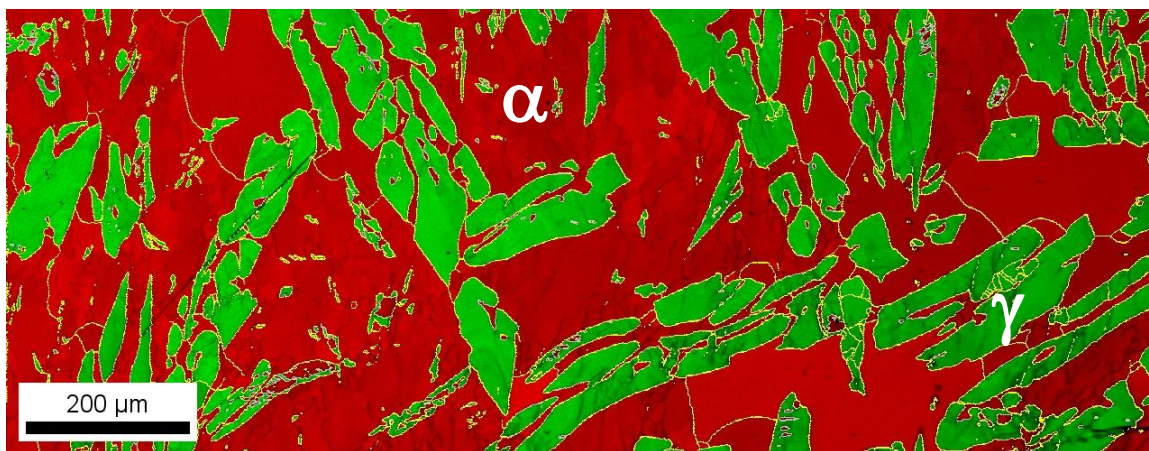
Boundaries: &lt;none&gt;



# Results – Hot deformation + Holding

## Microstructure - EBSD

$$T = 1150^{\circ}C, \quad \varepsilon = 0.3, \quad \dot{\varepsilon} = 1s^{-1}, \quad t_{\text{Holding}} = 3s$$



Color Coded Map Type: Phase

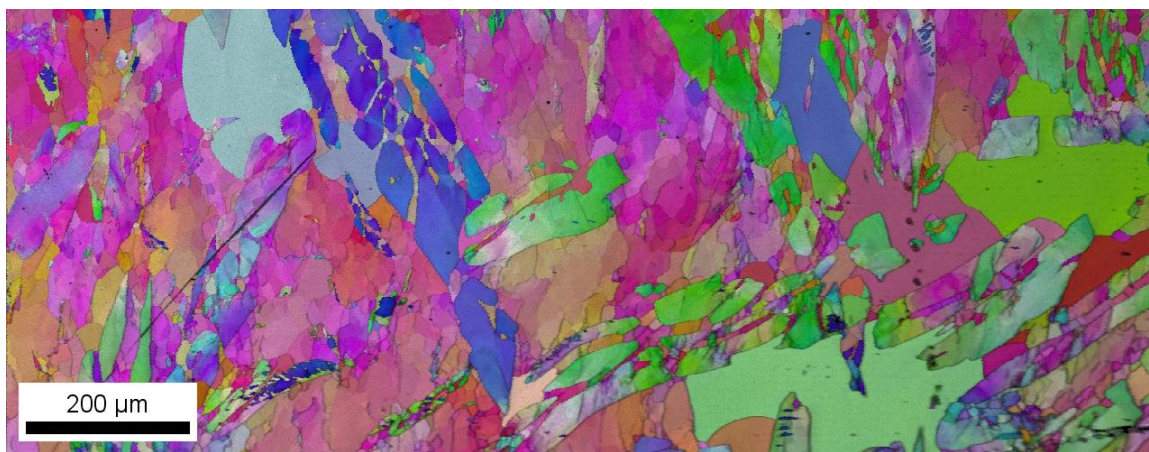
Phase	Total Fraction	Partition Fraction
Iron (Alpha)	0.658	0.658
Iron (Gamma)	0.342	0.342

Boundaries: Rotation Angle

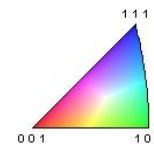
Min	Max	Fraction	Number	Length
15°	180°	0.471	94294	5.44 cm

Boundaries: Axis Angle

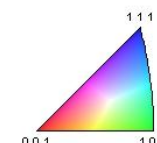
Plane Normal	Direction	Angle	Tolerance	Phase	Fraction	Fraction	Length
2 2 11	2 2 11	43°	5°	Iron (Alpha)	0.086	17163	9.91 mm



Iron - Alpha



Iron - Gamma



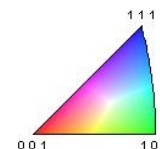
# Results – Hot deformation + Holding

## Microstructure Ferrite

$$T = 1150^{\circ}\text{C}, \quad \varepsilon = 0.3, \quad \dot{\varepsilon} = 1\text{s}^{-1}, \quad t_{\text{Holding}} = 3\text{s}$$

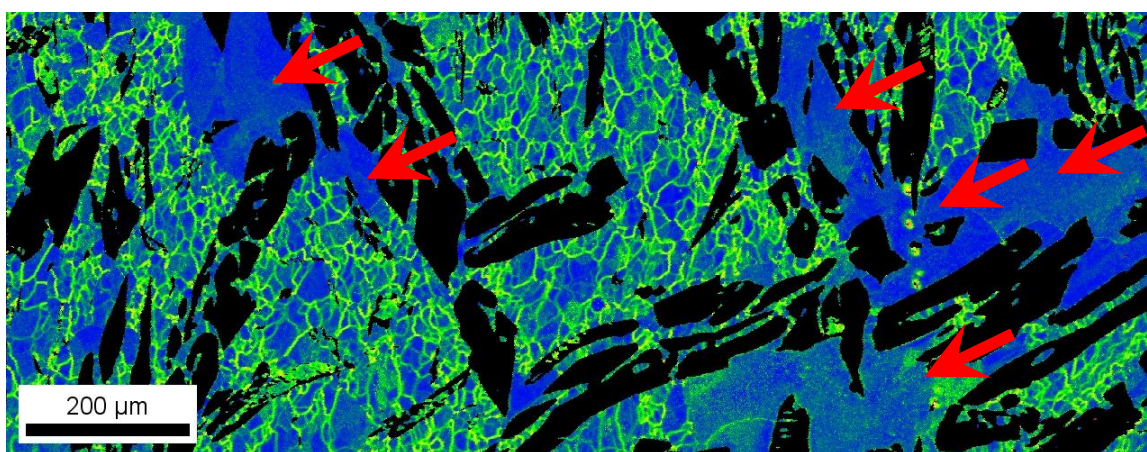


Color Coded Map Type: Inverse Pole Figure [001]  
Iron (Alpha)



Boundaries: Rotation Angle

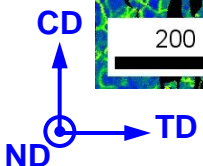
	Min	Max	Fraction	Number	Length
—	15°	180°	0.125	9745	5.63 mm
—	2°	14.9°	0.874	68162	3.94 cm



Color Coded Map Type: Kernel Average Misorientation

	Min	Max	Total Fraction	Partition Fraction
—	0	5	0.658	1.000

Boundaries: <none>



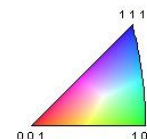
# Results – Hot deformation

## Microstructure Austenite

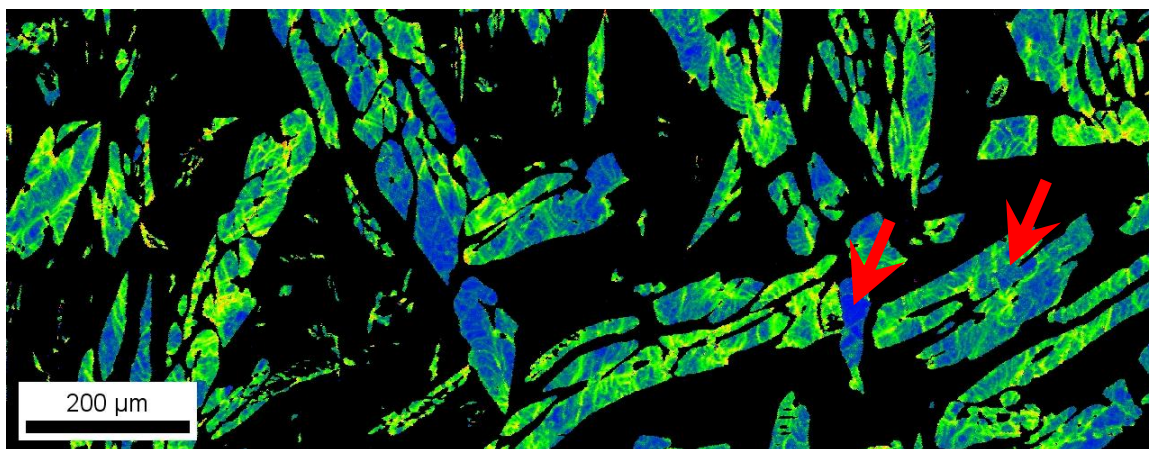
$$T = 1150^{\circ}C, \quad \varepsilon = 0.3, \quad \dot{\varepsilon} = 1s^{-1}, \quad t_{\text{Holding}} = 3s$$



Color Coded Map Type: Inverse Pole Figure [001]  
Iron (Gamma)



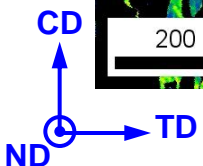
Boundaries: Rotation Angle					
	Min	Max	Fraction	Number	Length
—	2°	14.9°	0.907	37612	2.17 cm
—	15°	180°	0.092	3829	2.21 mm



Color Coded Map Type: Kernel Average Misorientation

	Min	Max	Total Fraction	Partition Fraction
—	0	5	0.342	1.000

Boundaries: <none>





# Summary

- morphology of phases (as cast): austenite islands in a ferrite matrix.
- austenite /ferrite: Kurdjumov-Sachs (K-S) orientation relationship.
- after deformation: ferrite shows dynamic recovery at high temperatures while the austenite is inhomogeneously deformed.
- deformation + holding time:
  - all temperatures  $\Rightarrow$  ferrite and austenite - static recovery.
  - high temperatures  $\Rightarrow$  ferrite and austenite - static recrystallization.

# Design of a novel Mn-based 1 GPa duplex stainless TRIP steel with 60% ductility by a reduction of austenite stability

C. Herrera, D. Ponge, D. Raabe\*

Max-Planck-Institut für Eisenforschung, Max-Planck-Strasse 1, 40237 Düsseldorf, Germany

Received 20 February 2011; received in revised form 29 March 2011; accepted 6 April 2011

Available online 3 May 2011

## Abstract

We report on the microstructure, texture and deformation mechanisms of a novel ductile lean duplex stainless steel (Fe–19.9Cr–0.42Ni–0.16N–4.79Mn–0.11C–0.46Cu–0.35Si, wt.%). The austenite is stabilized by Mn, C, and N (instead of Ni). The microstructure is characterized by electron channeling contrast imaging (ECCI) for dislocation mapping and electron backscattering diffraction (EBSD) for texture and phase mapping. The material has 1 GPa ultimate tensile strength and an elongation to fracture of above 60%. The mechanical behavior is interpreted in terms of the strength of both the starting phases, austenite and ferrite, and the amount, dispersion, and transformation kinetics of the mechanically induced martensite (TRIP effect). Transformation proceeds from austenite to hexagonal martensite to near cubic martensite ( $\gamma \rightarrow \varepsilon \rightarrow \alpha'$ ). The  $\varepsilon$ -martensite forms in the austenite with an orientation relationship close to Shoji–Nishiyama. The  $\alpha'$ -martensite nucleates at the intersections of deformation bands, especially  $\varepsilon$ -bands, with Kurdjumov–Sachs and Nishiyama–Wassermann relationships. The ferrite deforms by dislocation slip and contains cell substructures.

© 2011 Acta Materialia Inc. Published by Elsevier Ltd. All rights reserved.

**Keywords:** Stainless steels; High strength; Microstructure; Texture; EBSD

## 1. Introduction

Duplex stainless steels (DSS) which consist of ferrite and austenite (potentially plus corresponding displacive transformation products) are characterized by an excellent combination of good mechanical properties and corrosion resistance. The new alloy class proposed in this work uses Mn, C, and N (instead of only Ni) to stabilize the austenite (Fe–19.9Cr–0.42Ni–0.16N–4.79Mn–0.11C–0.46Cu–0.35Si, wt.%) [1–5]. Our design strategy aims at an alloying corridor to obtain optimum austenite stability. The motivation for that is twofold. First, the austenite should be sufficiently unstable that a transformation-induced plasticity (TRIP) effect is initiated upon loading. Second, the austenite should be sufficiently stable that the TRIP effect occurs over a wide strain regime, specifically at high strains, where strain hardening reserves are usually more desirable than at

low strains. The TRIP mechanism is based on deformation-stimulated displacive transformation of metastable austenite (face centered cubic Fe–Mn–N–C phase) to martensite (metastable or body centered orthorhombic ( $\alpha'$ ) or hexagonal ( $\varepsilon$ ) phase) and the matrix plus martensite plasticity required to accommodate the transformation misfit.

In the new alloy concept Mn not only replaces Ni but also increases the solubility of interstitial elements such as C and N, which promote austenite stabilization and provide additional solid solution strengthening [6]. N also enhances the resistance to localized corrosion and delays sensitization [7,8].

Commercial grade lean DSS (LDX 2101 and 1.4362,  $\sim$ Fe–22Cr–4Ni–0.3N–0.03C–0.3Mo, wt.%) exhibit a total elongation of up to 30% and ultimate strength levels of up to 600–700 MPa (Fig. 1). As well as these alloys with their limited ductility some studies have addressed improved lean DSS alloys [3,4]. Wang et al. [3] studied a new group of Ni-free, high strength and corrosion resistant DSS. These Ni-free alloys exhibited yield and ultimate

\* Corresponding author.

E-mail address: [d.raabe@mpie.de](mailto:d.raabe@mpie.de) (D. Raabe).

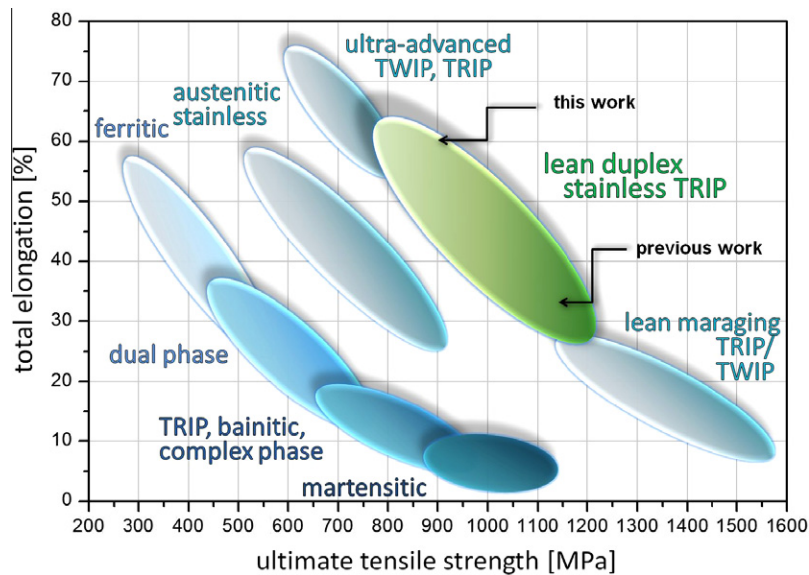


Fig. 1. Overview of total elongation to fracture vs. ultimate tensile strength for different steel grades.

tensile strengths of about 550 and 750 MPa, respectively, at an elongation to fracture of 40%. The materials exhibited excellent resistance to stress corrosion cracking (SCC) in chloride solutions. Wessman et al. [4] studied the effects of the replacement of Ni by Mn and N on the mechanical and corrosion properties in DSS alloys with up to 3 wt.% Mo. They found that the pitting corrosion resistance for the low and Ni-free alloys decreased while the yield stress and tensile stress increased with higher N and Mn contents. The effect of Ni on the mechanical properties was not significant.

The deformation behavior of DSS is complex. The ferrite ( $\alpha$ , bcc) deforms by slip due to the high stacking fault energy (SFE) and the numerous slip systems [9,10]. Austenite (fcc) can deform by different deformation modes, such as dislocation slip, mechanical twinning, or martensitic

transformations, plus the associated accommodation plasticity (TRIP) [7,11–18]. These deformation mechanisms lead to strong hardening and potentially also to excellent elongation, particularly when the TRIP effect is designed to occur over a wide load regime [12,13]. The latter deformation mode is affected by the austenite stability and the SFE, which both depend on the chemical composition and temperature [14,15]. Decreasing the SFE in the austenitic phase promotes twinning or martensitic transformation (TRIP effect) during deformation [14–18]. When the SFE is low perfect  $\{111\}\langle 110\rangle$  lattice dislocations dissociate into  $\{111\}\langle 112\rangle$  Shockley partial dislocations and stacking faults are formed between them. Deformation bands, which result from the collective and accumulated formation and motion of such planar defects, may form as a result of the overlapping of stacking faults on  $\{111\}$

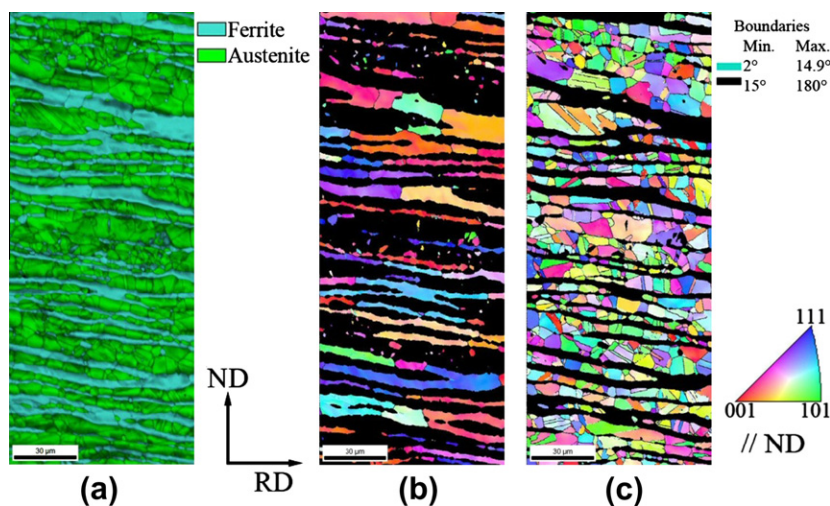


Fig. 2. EBSD maps: (a) IQ and phase distribution map; inverse pole figure and grain boundary distribution maps of (b) ferrite and (c) austenite of the ductile lean duplex stainless steel (hot rolled plus cold rolled plus heat treated for 5 min at 1050 °C).

planes in the austenite during deformation [12]. The deformation bands can be in the form of  $\varepsilon$  (hcp) martensite, mechanical twins, or dense stacking fault bundles [12,19,20]. Their formation is controlled by the SFE. A

low SFE energy favors the regular overlapping on every second  $\{111\}$  lattice plane and the formation of  $\varepsilon$ -martensite. The interaction of various such bands with  $\varepsilon$ -martensite zones promotes the formation of  $\alpha'$ -martensite nucleation [19,21]. The martensitic transformation in these materials hence typically follows the kinetic path  $\gamma \rightarrow \varepsilon \rightarrow \alpha'$  martensite [22,23].

The SFE of the austenitic phase in steels is well documented [14,15,24–27]. Schramm and Reed [24] determined that N, Cr, Si, and Mn decrease the SFE, whereas Ni and C increase it. For the austenitic phase of conventional Fe–Cr–Ni stainless alloys the SFE ranges from 10 to 100  $\text{mJ m}^{-2}$ . Reick et al. [28] found that the SFE of a high N Cr–Mn–Ni–Si austenitic stainless steel (Fe–16.5Cr–3Ni–8Mn–2Si–1Cu–0.25N, wt.%) was 16  $\text{mJ m}^{-2}$ . Not much experimental data on the SFE of the austenite phase in duplex stainless steels is available. Humphreys et al. [29] reported that the SFE of the austenite in DSS 1.4462 (Fe–22Cr–5Ni–3Mo–0.15–0.25N) was 10  $\text{mJ m}^{-2}$ . Recently, ab initio SFE predictions were published, although mainly on the Fe–Mn system [14,15].

The objective of this work is to study the deformation mechanisms and the phase transformation behavior of a new type of Mn and N alloyed lean DSS. The concentration of these elements was optimized in order to enhance both strength and ductility through an optimal design of the instability of the austenitic phase with respect to promotion of the TRIP effect up to high deformations. Detailed microstructural characterization by electron channeling contrast imaging (ECCI) for dislocation and twin imaging and electron backscatter diffraction (EBSD) for texture and phase maps was performed on tensile deformed samples at room temperature at different strains. The aim is to identify the reasons for the excellent strength and ductility profile observed in this material, exceeding the properties observed so far in other duplex steels.

## 2. Experimental

A DSS with composition Fe–19.9Cr–0.42Ni–0.16N–4.79Mn–0.11C–0.46Cu–0.35Si (wt.%) was prepared in a laboratory vacuum induction furnace under 200 Mbar Ar pressure. The cast ingot was reheated to 1200 °C for 30 min, hot rolled from 40 to 3 mm, and water quenched. The material was then cold rolled from 3 to 1 mm, followed by recrystallization at 1050 °C for 5 min, and final water quenching.

Interrupted tensile tests were carried out to different strains. Flat tensile specimens were machined parallel to the rolling axis with a cross-section of  $1 \times 8$  mm and a gage length of 30 mm. Tests were conducted in a Zwick ZH 100 tensile machine at room temperature with a constant cross-head speed, i.e. at an initial strain rate of  $8 \times 10^{-1} \text{ s}^{-1}$ .

Samples were examined by ECCI and EBSD using a field emission gun scanning electron microscope.

Samples for microstructural investigations were prepared as longitudinal sections by standard mechanical

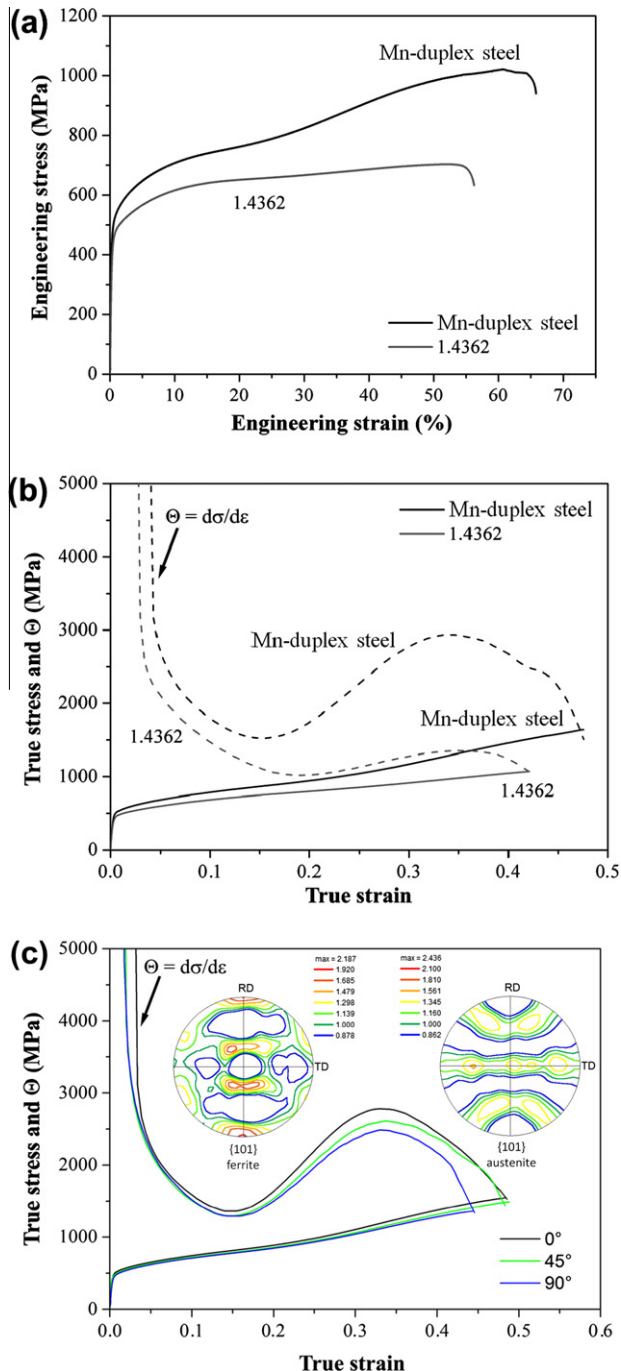


Fig. 3. The (a) engineering stress–strain curve and (b) strain hardening rate of the new lean duplex stainless steel and, for comparison, of the standard alloy 1.4362. Initial strain rate  $8 \times 10^{-1} \text{ s}^{-1}$ . (c) The same analysis for specimens cut in three different directions relative to the former rolling direction ( $0^\circ$ ,  $45^\circ$ , and  $90^\circ$ ). The results reveal a small dependence of the mechanical properties on the texture, i.e. a small mechanical anisotropy. The conventional duplex stainless steel 1.4362, which is shown as a reference material in (a and b), has the exact composition Fe–22Cr–3.6Ni–1.4Mn–0.024C–0.4Cu (wt.%).

grinding and polishing procedures. In the final step samples were electropolished using Struers electrolyte A3 at room temperature (18 V, flow rate of  $10 \text{ s}^{-1}$ ). The EBSD technique was used to determine the phase ratio, crystallographic texture, interface character and substructure characteristics. The EBSD scans were carried out at 15 kV in the middle of the samples at a step size of 100 nm. Additional high resolution EBSD maps were taken at 50 and 30 nm step sizes, respectively. The raw data were post-processed using TSL OIM software. An EBSD map is characterized by its crystallographic orientation,

confidence index (CI), and image quality (IQ). The CI is a measure of the reliability of the diffraction pattern indexing. The IQ quantifies the sharpness of the diffraction bands. It can serve as a qualitative measure of crystal perfection in terms of its lattice defect content. Perfect crystal regions have a high IQ (light) while regions with a high defect density (e.g. adjacent to interfaces, severely deformed zones, inclusions, etc.) have a lower IQ (dark) [29]. While identification of the fcc phase (austenite) via EBSD is straightforward, differentiation among the two bcc phases, i.e. ferrite and martensite, is more challenging.

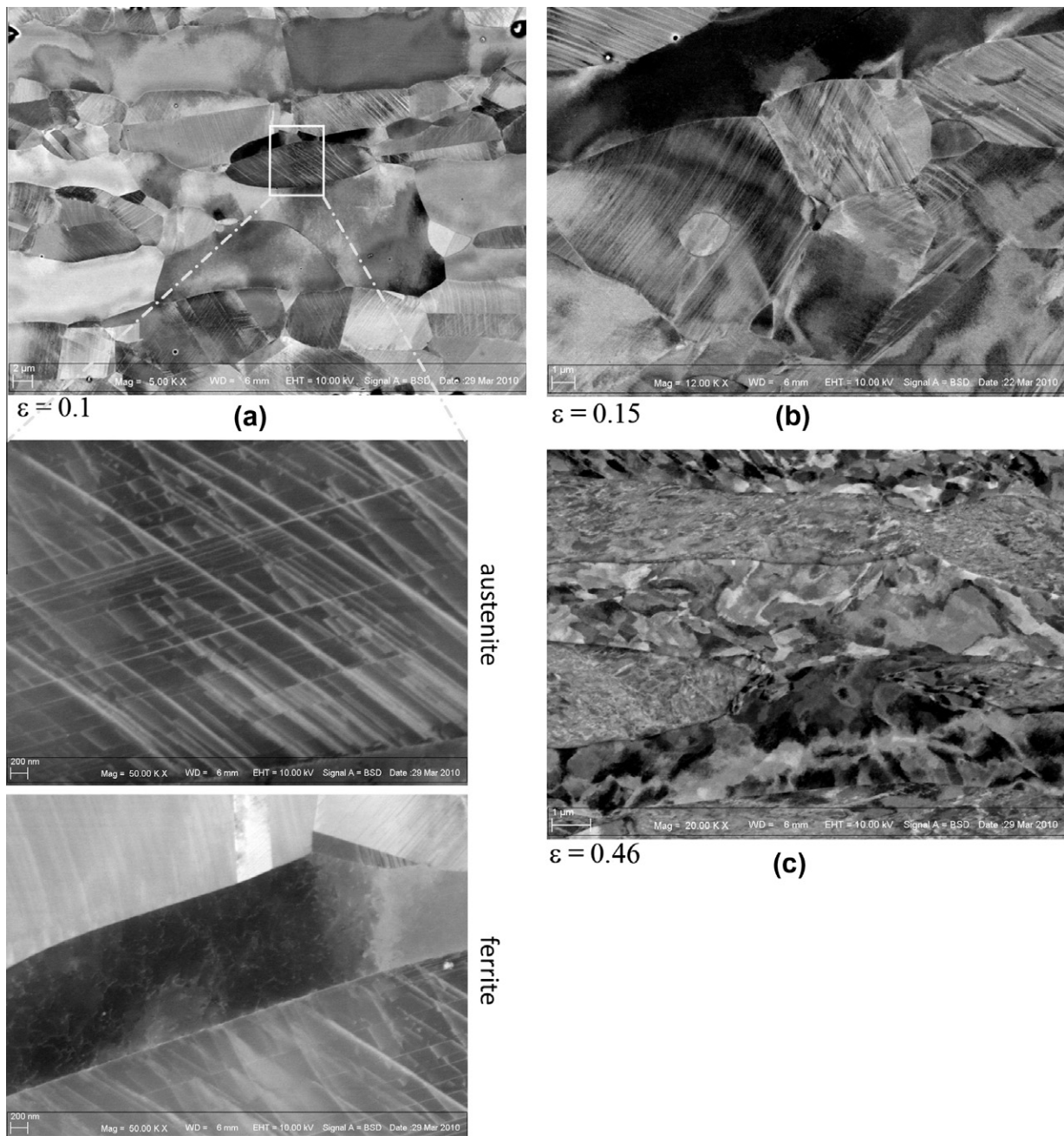


Fig. 4. Deformation microstructure of the new lean duplex stainless steel tensile strained to true plastic strains of (a) 0.1, (b) 0.15 and (c) 0.46. The images were taken using the ECCI method. Initial strain rate  $8 \times 10^{-1} \text{ s}^{-1}$ .

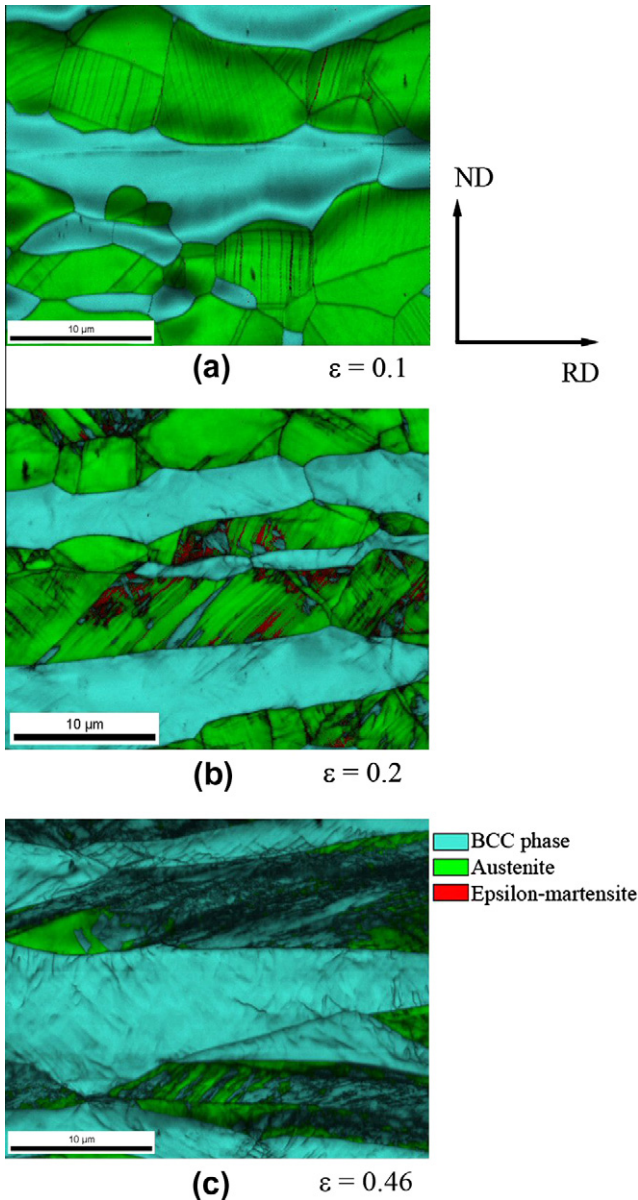


Fig. 5. Evolution of the microstructure of the new ductile lean duplex stainless steel deformed to logarithmic strains of (a) 0.1, (b) 0.2 and (c) 0.46. bcc phase: ferrite and  $\alpha'$ -martensite. The differentiation between the two phases is possible using the image quality (IQ) as an additional indicator of the internal defect structure.

The IQ and CI values have been used to distinguish the two phases in previous works [30,31]: The martensite shows lower IQ and CI values, due to a higher density of lattice defects. The average misorientation of a given point relative to its neighbors is calculated using an orientation gradient kernel approach. Here the kernel average misorientation (KAM) was calculated up to the fifth neighbor shell with a maximum misorientation angle of  $2^\circ$ . EBSD maps are displayed as phase distribution and IQ (phase plus IQ) maps, phase maps including the boundary character between the phases, inverse pole figure (IPF) maps, and KAM maps of each phase (bcc, i.e. ferrite ( $\alpha$ ) and  $\alpha'$ -martensite, austenite, and  $\epsilon$ -martensite).

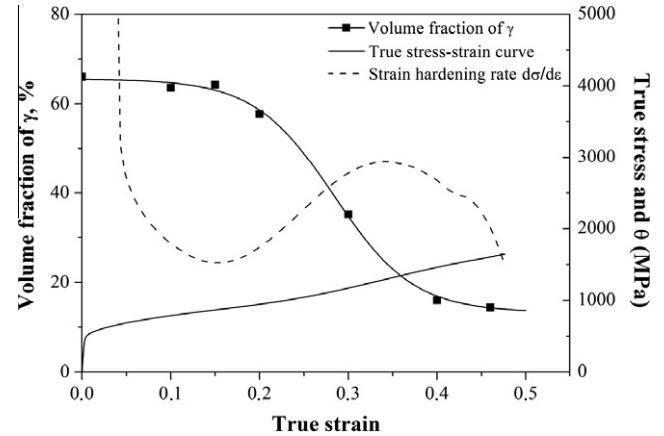


Fig. 6. Volume fraction of austenite as a function of the true plastic strain, plotted together with the true stress–strain curve and the strain hardening rate for the new lean duplex stainless steel.

The recently improved scanning electron microscopy (SEM)-ECCI technique [32–38] is used to image microstructural features that are not well captured by EBSD, such as single dislocations, dislocation substructures (e.g. cells), twins, grain boundaries and deformation bands. The specific advantage of the ECCI method in that context is that it provides a large field of view [37]. The fact that this method works in SEM rather than transmission electron microscopy renders the ECCI approach suitable for large-scale and statistical mapping of microstructures at the grain and subgrain scale [38]. ECCI was carried out in a Zeiss Crossbeam instrument equipped with a Gemini field emission gun (FEG) column at an acceleration voltage of 10 kV and a working distance of 6 mm.

### 3. Experimental results

Fig. 2 shows the microstructure of the material after thermomechanical processing, consisting of hot rolling, cold rolling, and subsequent recrystallization annealing treatment.

The figure reveals a completely recrystallized “bamboo”-type microstructure for both phases, where the grain boundaries extend perpendicular to the phase boundaries. The morphology of the crystals is inherited from the preceding rolling procedures, revealing the characteristic elongated, alternating layered structure of austenite and ferrite. The austenite exhibits a smaller grain size than the ferrite and contains annealing twins. The ferrite does not show any internal substructure in the EBSD maps and has much larger grains and a more pronounced “bamboo”-type microstructure compared with the austenite. The volume fractions, determined by EBSD, are 37 vol.% ferrite and 63 vol.% austenite. The crystallographic texture of both phases is weak.

The engineering stress–strain curves of the new Mn–N DSS and, for comparison, of a conventional DSS 1.4362 with the exact composition Fe–22Cr–3.6Ni–1.4Mn–0.024C–0.4Cu (wt.%) are shown in Fig. 3a. An increase

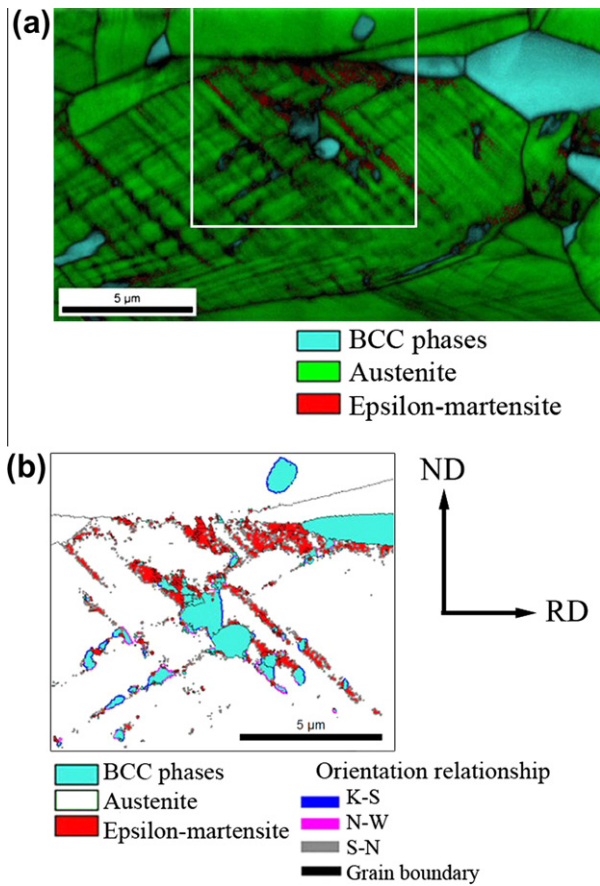


Fig. 7. Microstructure of the Mn-based duplex stainless steel tensile deformed to a logarithmic strain of 0.15. (a) IQ and phase distribution map; (b) magnification of the area marked in (a) showing the local orientation relationships and the phase distribution map. S–N, Shoji–Nishiyama; K–S, Kurdjumov–Sachs; N–W, Nishiyama–Wassermann.

in the yield strength from 400 to 500 MPa and of the ultimate tensile strength from 790 to 1020 MPa is observed for the new alloy compared with the conventional one. This improvement is surprisingly accompanied by an increase in the elongation to failure from 50% to nearly 65% for the new alloy. Fig. 3b shows the true stress vs. strain curves together with the strain hardening rates for the two alloys. The true stress–strain curves show a sigmoidal behavior. The strain hardening curve of the new steel displays a multiple stage strain hardening behavior. The first parabolic strain hardening regime monotonically decreases to a strain of about 0.15 where the strain hardening curve assumes a minimum of about 1500 MPa. Beyond this point the strain hardening curve increases with further straining and reaches a level of 2500 MPa at a strain of about 0.35. Then the strain hardening rate decreases rapidly to the intersection with the true stress–strain curve. The strain hardening curve of the reference alloy 1.4362 shows a profoundly weaker strain hardening behavior. In particular, the second strain hardening plateau occurring after the minimum in strain hardening at a true strain of

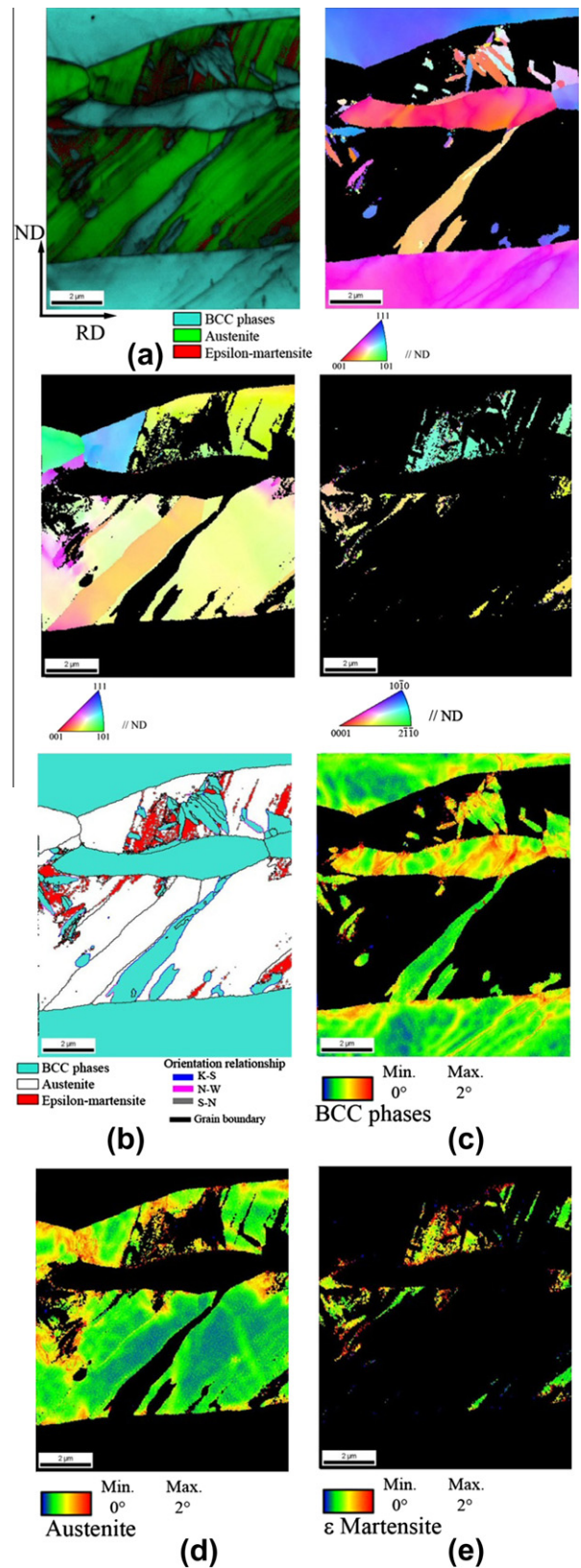


Fig. 8. EBSD maps of the Mn-based duplex stainless steel tensile deformed to a logarithmic strain of 0.2. (a) IQ and phase distribution, (b) orientation relationships; IPF and KAM maps of (c) bcc phase (ferrite plus α-martensite), (d) austenite, and (e) ε-martensite. S–N, Shoji–Nishiyama; K–S, Kurdjumov–Sachs; N–W, Nishiyama–Wassermann.

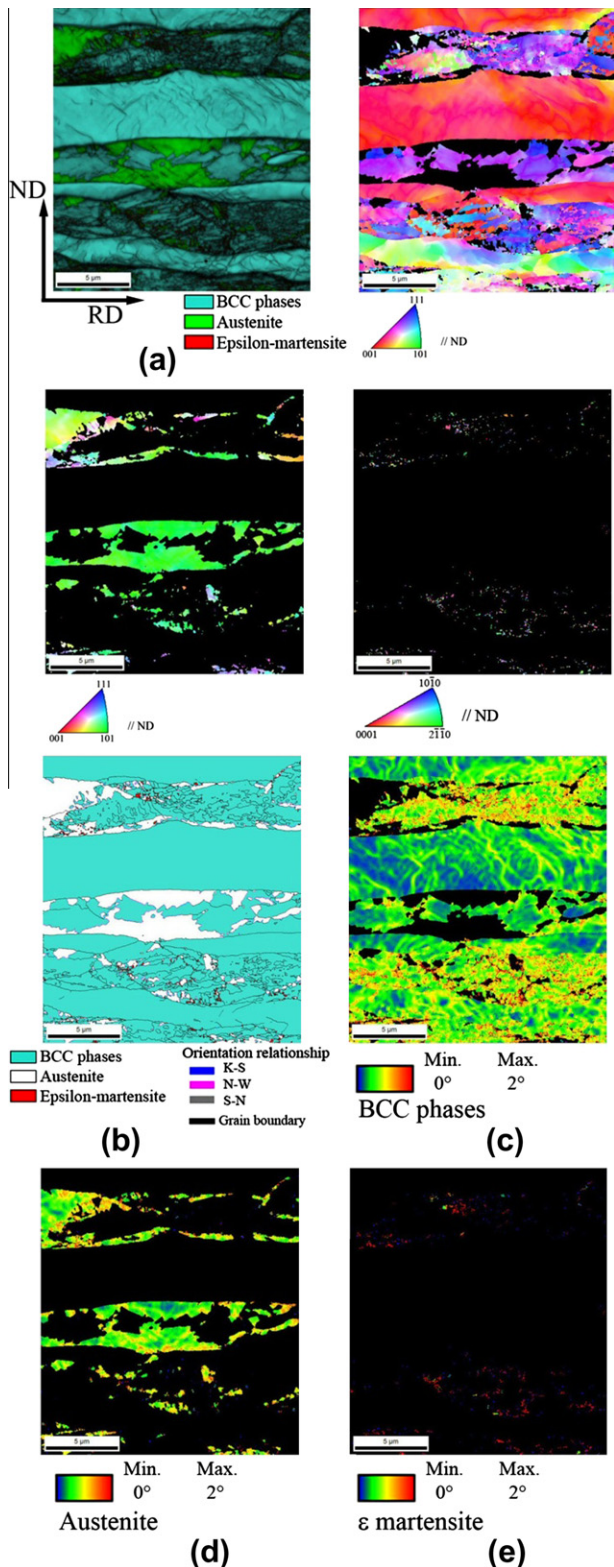


Fig. 9. EBSD maps of the Mn-based duplex stainless steel tensile deformed to a logarithmic strain of 0.46. (a) IQ and phase distribution; (b) orientation relationship; IPF and KAM maps of (c) bcc phase (ferrite plus  $\alpha'$ -martensite), (d) austenite, and (e)  $\epsilon$ -martensite. S–N, Shoji–Nishiyama; K–S, Kurdjumov–Sachs; N–W, Nishiyama–Wassermann.

about 0.2 is much weaker than that observed in the new Mn–N alloy. The crystallographic texture and the result-

ing mechanical anisotropy of the material are weak: Fig. 3c shows that the stress vs. strain and the strain hardening curves of the new alloy taken in three different directions relative to the rolling direction ( $0^\circ$ ,  $45^\circ$ , and  $90^\circ$ ) reveal only minor differences.

The transitions in the strain hardening behavior revealed in Fig. 3b and c result from changes in the deformation mechanisms. Fig. 4 shows the ECCI images of the microstructure evolution of the new Mn–N duplex steel deformed in tension to true strains of 0.1, 0.15, and 0.46 at room temperature. At a low strain and stress level ferrite and austenite reveal differences in their deformation microstructures. The ferrite microstructure is characterized by tangled dislocations and slightly misoriented cells within the original grains. At higher deformations the ferrite microstructure is more heavily deformed and the dislocation density increases. The ECCI images of the austenite grains reveal not only parallel and multiple intersecting deformation bands but also the formation of a cell structure at lower strains. With increasing deformation the density of deformation bands in the austenite increases. At higher strains the shear bands and cells structure in the austenitic crystals cannot be clearly identified any more. A clear differentiation between substructure features, such as twins or  $\epsilon$ - and  $\alpha'$ -martensite, is only possible by combining the ECCI and EBSD techniques.

Fig. 5 shows the microstructure evolution in terms of superimposed phase plus IQ maps of the new lean DSS strained to 0.1, 0.2 and 0.46 logarithmic strain at room temperature. The three phases, austenite,  $\epsilon$ -martensite and the bcc phase (ferrite plus  $\alpha'$ -martensite) are represented by a specific color code according to the legend, while the gray values quantify the IQ. The ferrite and  $\alpha'$ -martensite, both with a bcc or near-bcc lattice structure (blue), were discriminated using the IQ values. The martensite contains a higher number of lattice defects and thus leads to lower IQ values. At low strain ( $\epsilon = 0.1$ ) the austenite (green) shows a heterogeneous distribution of the deformation bands, which have a lower IQ factor due to distortion of the lattice. A few of these bands were identified as  $\epsilon$ -martensite (red). The  $\alpha'$ -martensite is not directly identified as a separate phase by the EBSD technique and hence for identification requires combination with the IQ values. The ferrite phase is characterized by a lower deformation compared with martensite. When the strain increases the density of the deformation bands in the austenite increases and deformation band intersection occurs. The density of deformation bands that are indexed as  $\epsilon$ -martensite also increases. The  $\alpha'$ -martensite was identified due to a low IQ value. It is observed to nucleate in the intersection of the deformation bands, especially at the  $\epsilon$ -martensite intersections, or in regions near to annealing twins or grain boundaries. The ferrite contains dislocation cells. Ferrite regions close to  $\alpha'/\gamma$  boundaries are more deformed compared with ferrite grain interiors. At the maximum true strain (0.46) almost all of the austenite has transformed into  $\alpha'$ -martensite, which shows a very

high dislocation density. This process, i.e. the gradual and nearly complete transformation of the austenite (only 10 vol.% remains) to martensite is an essential ingredient in the optimal strain hardening design of the new material. The  $\varepsilon$ -martensite at this stage can no longer be identified, as it has also been transformed into  $\alpha'$ -martensite. The ferrite is characterized by a heavily deformed microstructure with a pronounced cell substructure.

Fig. 6 shows the volume fraction of austenite measured via EBSD as a function of the true plastic strain. The volume fraction of austenite decreases continuously with increasing strain due to  $\varepsilon$ - and  $\alpha'$ -martensite transformation (TRIP effect). The martensite content reaches a saturation value before the maximum uniform elongation is achieved.

Fig. 7 shows a highly magnified austenite grain and its surrounding matrix. The sample is strained to 0.15. The combined phase plus IQ map (Fig. 7a) reveals that the deformation bands consist of  $\varepsilon$ -martensite and stacking faults. The  $\varepsilon$ -martensite is formed by overlapping stacking faults and, therefore, is finely dispersed [19]. It has an orientation relationship close to the Shoji–Nishiyama (S–N) relation,  $(1\ 1\ 1)\gamma \parallel (0\ 0\ 0\ 1)\varepsilon$  and  $[1\ 0\ \bar{1}]\gamma \parallel [1\ 1\ \bar{2}\ 0]\varepsilon$ , to the austenite grains [21]. The  $\alpha'$ -martensite nucleates in the intersection of the  $\varepsilon$ -bands and in regions close to it, as

has also been observed by other groups in austenitic stainless steels [13,19,21,30,31]. The  $\alpha'$ -martensite can assume different morphologies, such as lath or block shapes. The orientation relation between austenite and  $\alpha'$ -martensite is characterized by the Kurdjumov–Sachs (K–S), i.e.  $(1\ 1\ 1)\gamma \parallel (1\ 1\ 0)\alpha'$  and  $[\bar{1}\ 0\ 1]\gamma \parallel [1\ \bar{1}\ 1]\alpha'$ , and Nishiyama–Wassermann (N–W) relationships, i.e.  $(1\ 1\ 1)\gamma \parallel (0\ 1\ 1)\alpha'$  and  $[1\ 1\ 2]\gamma \parallel [0\ 1\ 1]\alpha'$ .

Fig. 8 shows the deformation microstructure of the new alloy deformed to a logarithmic strain of 0.2. Fig. 8a and b shows the phase plus IQ map and the phase distribution containing the grain boundary character. Fig. 8c–e shows the IPF and KAM maps of each phase, namely of the bcc phase (ferrite plus  $\alpha'$ -martensite), austenite, and  $\varepsilon$ -martensite. The KAM maps serve as a measure of the deformation-induced local orientation gradients inside grains. The map of the deformed ferrite (blue) shows a substructure consisting of cells or subgrains. Regions with a low IQ inside the ferrite grains can be defined as dislocation walls. The ferrite crystals exhibit in-grain orientation gradients which are related to the formation of geometrically necessary dislocations and cell formation (Fig. 8c). The KAM map of ferrite shows that the highest local misorientations are located at the  $\alpha/\alpha$  and  $\alpha/\gamma$  interfaces and at the in-grain cell boundaries, where high dislocation densities prevail.

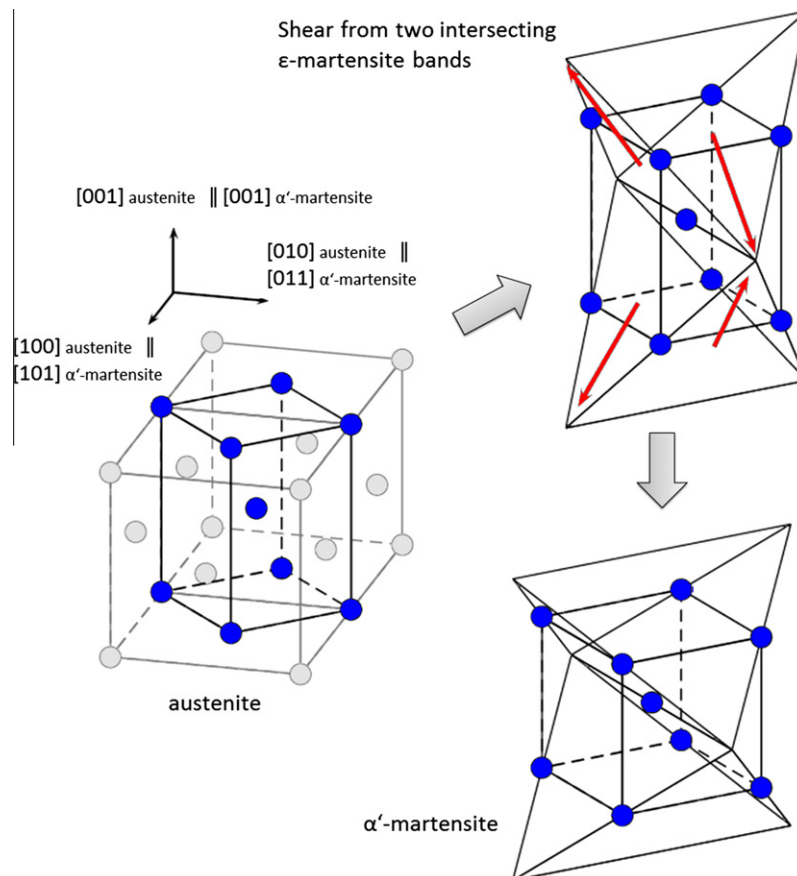


Fig. 10. Schematic drawing explaining the effect of the superimposed shear that is created by two intersecting  $\varepsilon$ -martensite bands. The total distortion imposed on the fcc austenite lattice by the intersecting  $\varepsilon$ -martensite bands shifts the crystal structure to close to that of  $\alpha'$ -martensite.

The austenite (green) in Fig. 8 exhibits a heterogeneously deformed microstructure and deformation bands. Within the austenite grains  $\varepsilon$ - (red) and  $\alpha'$ - (blue) martensite phases were identified. The KAM map (Fig. 8d) shows the local orientation gradients inside the austenite grains. The dislocation density distribution becomes strongest close to the annealing twins, the ferrite/austenite and  $\varepsilon$ - and  $\alpha'$ -martensite/austenite interfaces. The  $\varepsilon$ -martensite has a close to S–N relationship with the austenite. The  $\alpha'$ -martensite grows with K–S and N–W orientation relationships with a lath morphology.

At the maximum uniform strain ( $\varepsilon \approx 0.46$ ) all phases present are heavily deformed (Fig. 9). The ferrite shows a heterogeneous dislocation distribution. Most of the austenite has transformed into  $\alpha'$ -martensite ( $\sim 10$  vol.% remaining), which after the transformation process exhibits a high dislocation density. The remaining austenite is highly deformed. The  $\alpha'$ -martensite presents a complex microstructure with increasing strain, i.e. heavily deformed areas without specific morphological features and others with block or lath-type morphologies can be observed. The volume fraction of  $\varepsilon$ -martensite decays with increasing strain owing to gradual transformation of  $\varepsilon$ - to  $\alpha'$ -martensite.

#### 4. Discussion

The plastic response of the Mn-based DSS is characterized by the individual deformation behavior of the four phases  $\gamma$  (austenite),  $\alpha$  (ferrite),  $\alpha'$ -martensite, and  $\varepsilon$ -martensite, the deformation-induced transformation from austenite to  $\varepsilon$ -martensite and further to  $\alpha'$ -martensite, and the micromechanical interactions among these phases.

At the onset of loading plastic deformation is first concentrated within the austenitic phase. These grains deform heterogeneously, as is evident from the high density of deformation bands that appear inside the grains and also extend into neighboring crystals (Figs. 5, 8 and 9). In contrast, the ferritic phase, which has a high number of potential slip systems ( $\langle 111 \rangle \{110\}$ ,  $\langle 111 \rangle \{112\}$ ) shows a cell substructure rather than a banded-type morphology. This difference in substructure between austenite and ferrite is also confirmed by direct mapping of the dislocation substructure via ECCI (Fig. 4a). Zones of high deformation accumulation are mainly observed close to the interfaces between the two phases  $\gamma$  and  $\alpha$ , and also at the cell walls.

Microstructural characterization reveals that the  $\varepsilon$ -martensite is distributed heterogeneously along shear zones in the austenite grains (Figs. 5b and 7). The volume fraction of  $\varepsilon$ -martensite grows with increasing strain, although after formation it is quickly further transformed into  $\alpha'$ -martensite. The  $\alpha'$ -martensite zones are located at the intersections, particularly of those deformation bands which were indexed as  $\varepsilon$ -martensite (Fig. 7b).

The  $\varepsilon$ -martensite has a near S–N orientation relationship,  $(111)\gamma \parallel (0001)\varepsilon$  and  $[10\bar{1}]\gamma \parallel [1\bar{2}0]\varepsilon$ , to the austenite (Fig. 10). This orientation relationship is characterized by the coincidence of the close packed fcc and hcp crystal

structures [21]. The  $\alpha'$ -martensite nucleates in the intersection of the  $\varepsilon$ -bands and in regions close to it (Fig. 7b). This observation matches previous results in austenitic steels [13,19,21,30,31,39,40]. The orientation relation between austenite and  $\alpha'$ -martensite is characterized by the K–S, i.e.  $(111)\gamma \parallel (110)\alpha'$  and  $[\bar{1}01]\gamma \parallel [1\bar{1}1]\alpha'$  and N–W relationships, i.e.  $(111)\gamma \parallel (011)\alpha'$  and  $[112]\gamma \parallel [011]\alpha'$  [31].

These results suggest that the austenite transforms to  $\alpha'$ -martensite following the sequence  $\gamma \rightarrow \varepsilon \rightarrow \alpha'$ . This means that a direct relation exists between  $\varepsilon$ -martensite, aligned along transformed former austenite deformation bands, and the nucleation of  $\alpha'$ -martensite inside the crossing points of such  $\varepsilon$ -bands. This transformation sequence was originally discussed by Olson and Cohen [19,21]. The model suggests that the superimposed shear created by two intersecting  $\varepsilon$ -martensite bands leads to a total distortion that shifts the original austenite lattice close to the final  $\alpha'$ -martensite structure (Fig. 10).

Another important observation regarding the evolution of the substructure and its possible relevance to an understanding of the mechanical behavior is the distribution of the KAM values of the deformed samples (Fig. 11). The

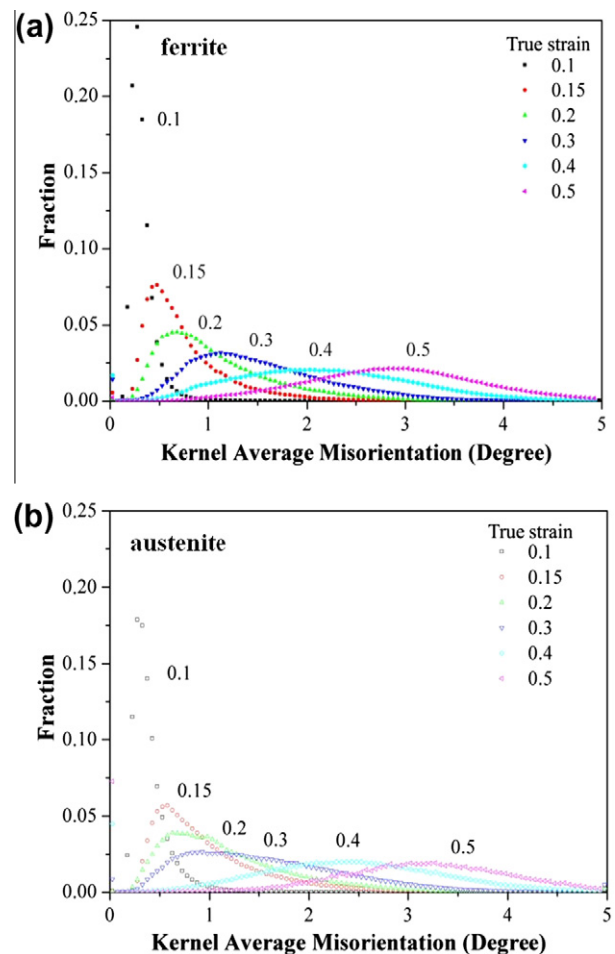


Fig. 11. KAM distributions with various deformations of (a) the bcc phase (ferrite +  $\alpha'$ -martensite) and (b) austenite. KAM, kernel average misorientation.

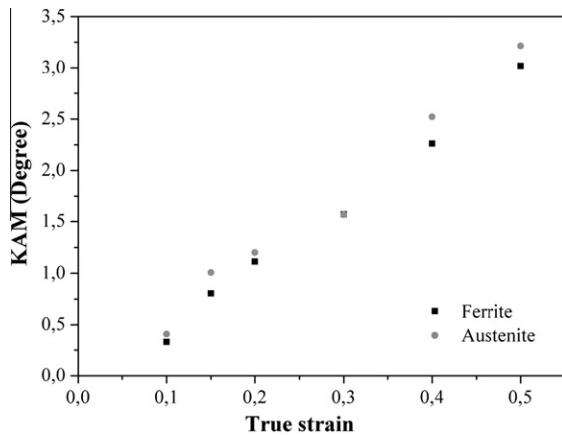


Fig. 12. Average KAM as a function of deformation strains for the bcc phase (ferrite +  $\alpha'$ -martensite) and austenite. KAM, kernel average misorientation.

evolution of the KAM distribution is similar for both phases, austenite and ferrite plus martensite. At low strains the KAM distribution reveals small average values for both phases. This indicates a low dislocation density and a narrow misorientation distribution [41–43]. The ferrite contains a slightly higher fraction of small in-grain misorientations than the austenite. With increasing strain the curves shift towards higher average misorientation angles due to an increase in the dislocation density and in-grain structure evolution [44]. The average misorientation values increase with strain in both phases (Fig. 12). At higher strains the austenite reveals slightly higher average KAM values than the ferrite. This is mainly attributed to the fact that the austenite accumulates more deformation than the bcc phase, where the martensite in particular is much stronger than the austenite, so that the strain concentrates in the austenite.

The main question now is how these different observations on the substructure and transformation sequence help us to better understand the mechanical behavior of the material, more specifically, its excellent ductility-strength combination compared with conventional DSS alloys (Figs. 3 and 6).

In that context it is important to discuss in more detail the volume fraction of austenite, measured via EBSD, as a function of the true plastic strain (Fig. 6) [45–47]. The drop in austenite fraction shows a sigmoidal form due to the  $\epsilon$ - and  $\alpha'$ -martensite transformation sequence that occurs with increasing strain, as discussed above. It is important to note that the martensite content reaches a saturation value at around the true strain value, where the maximum uniform elongation is achieved (Fig. 6). This observation indicates that the increase in work hardening rate at intermediate strains is controlled by the formation of strain-induced  $\alpha'$ -martensite rather than by the dislocation substructure evolution, as for instance indicated by the change in the average in-grain misorientation pattern in ferrite and austenite.

The strain at which the  $\alpha'$ -martensite starts to form at intersecting  $\epsilon$ -martensite bands was referred to as transient strain by Stringfellow et al. [48]. In the strain hardening curve (Fig. 6) the inflexion point where the curve changes its behavior from a parabolic to sigmoidal shape marks this transient strain regime, which in the current case is close to 0.15. Even before this transient strain  $\epsilon$ -martensite has gradually been formed (Fig. 7b), but does not change the overall strain hardening curve behavior of the material. The volume fraction of austenite starts to decrease significantly at about this strain, as confirmed by Fig. 6.

These observations suggest that the formation of strain-induced  $\alpha'$ -martensite primarily promotes the enhancement of both strength and ductility through a TRIP effect.

Additionally the solid solution hardening effect, specifically of N, C, and Mn, plays an important role, at least for the high strength level of the material, since the retained austenite phase (and, hence, also the deformation-induced martensite) in the new alloy contains more of these elements than conventional DSS. In the reference alloy (1.4362) the role of C and N in solid solution strengthening is assumed to be lower than in the new lean alloy, because the austenite design in conventional DSS is achieved by Ni. This element decreases the solubility of the interstitial elements (C and N), while Cr and Mn have an opposite effect and increase their solubility. Altogether this yields a higher interstitial solid solution hardening effect in the new steel.

The main effect of N, C, and Mn, however, lies in their influence on austenite stability, which is dependent on the chemical composition and temperature [22]. Properly designing the stability of the austenite phase against deformation-stimulated transformations is essential. In conventional steels containing unstable austenite displacive transformations (twinning, martensite formation) and the associated strain hardening response via the TRIP or TWIP effects often occur only in the early stages of deformation, where additional hardening is usually not needed and the austenite often only partially transforms into  $\alpha'$ -martensite. In contrast, the design strategy in the current case aims at optimizing the corridor for austenite stability according to two bounds. On the one hand, the austenite should be sufficiently unstable to initiate a TRIP effect upon mechanical loading and transform most of its volume into martensite. On the other hand, it should be sufficiently stable that the transformation process extends over a wide stress-strain regime up to higher deformations where additional strain hardening is usually more important than at low strains, as it then provides a more continuous increase in strength during straining.

The stability design of the austenite against deformation-stimulated martensite formation is in the current case essentially achieved via C, N, and Mn alloying (in addition to the minor Ni content). The effect of the different solute elements on austenite stability can be described in terms of the  $Md_{30}$  temperature. Angel [50] defined the  $Md_{30}$  value as the temperature at which half of the austenite is transformed into martensite through a cold-deformation step

to a logarithmic strain of 0.30 (~35% engineering strain). A low  $Md_{30}$  temperature indicates high austenite stability against the formation of deformation martensite. It can be estimated by various empirical equations available in the literature [49–52]. The  $Md_{30}$  temperature [50], calculated from Eq. (1), is 64.0 °C for the austenite phase in the new Mn DSS and 28.1 °C for the austenite phase in the conventional reference alloy 1.4362.

$$\begin{aligned} Md(\gamma) = & 551 - 462(C(\gamma) + N(\gamma)) - 9.2Si(\gamma) \\ & - 8.1Mn(\gamma) - 13.7Cr(\gamma) - 29Ni(\gamma) \\ & - 29Cu(\gamma) - 18.5Mo(\gamma) \end{aligned} \quad (1)$$

For this purpose the chemical composition of the austenite at 1050 °C was determined for both materials using ThermoCalc version S in conjunction with the TCS Steels/Fe-alloys database v. 6. The stability values predicted by Eq. (1) can only serve as a guideline, since we used the composition of the austenite in the equilibrium (rather than transient) state that Thermocalc predicts. For this reason we do not use the current equation for quantitative statements but only to identify trends in austenite stability. According to this estimate the reference alloy 1.4362 has the lower  $Md_{30}$  temperature, i.e. exhibits higher austenite stability compared with the new Mn-based duplex alloy. This means that the kinetics and completeness of the deformation-stimulated transformation from austenite into martensite and the resulting TRIP effect are better promoted in the new alloy as opposed to the reference alloy.

## 5. Conclusions

The microstructure and deformation mechanisms of a novel high strength (1 GPa ultimate tensile strength) and highly ductile (>60% elongation to fracture) lean Mn-based duplex stainless TRIP steel were analyzed and discussed (Fe–19.9Cr–0.42Ni–0.16N–4.79Mn–0.11C–0.46Cu–0.35Si, wt.%). The results were compared with those observed for a conventional DSS (LDX 2101, 1.4362, Fe–22Cr–4Ni–0.3N–0.03C–0.3Mo, wt.%). The main observations and conclusions are as follows.

- The ferrite deforms by slip and develops cell substructures.
- The austenite deforms by dislocation glide, deformation banding, and deformation-induced martensitic transformations according to  $\gamma \rightarrow \varepsilon \rightarrow \alpha'$ . This sequence agrees with the Olson–Cohen model, i.e. nucleation of  $\alpha'$ -martensite occurs at the intersections of deformation bands, especially at intersections of two  $\varepsilon$ -bands or  $\varepsilon$ -bands with twins or grain boundaries.
- The orientation relationship between  $\varepsilon$ -martensite and austenite is close to the S–N relationship, while  $\alpha'$ -martensite and austenite showed K–S and N–W relationships.
- At lower strains  $\alpha'$ -martensite shows a lath morphology, but the structure becomes more irregular with increasing strain.
- The excellent strength–ductility profile of the new material is mainly attributed to the TRIP effect that is associated with the  $\alpha'$ -martensite transformation. The TRIP effect in this material enhances strain hardening over a wide deformation regime and, hence, the ductility of the steel. The specific beneficial effect of Mn, C, and N alloying is attributed to the fact that these elements increase the  $Md_{30}$  temperature (64.0 °C) of the new alloy compared with that of conventional duplex stainless steels (28.1 °C). This leads to an easier activation of deformation-stimulated martensite transformation and hence of the TRIP effect and also to more complete and gradual transformation kinetics of the austenite up to higher deformation levels where conventional duplex stainless steels are plastically exhausted and affected by localization and damage initiation.

## References

- [1] Charles J. Steel Res Int 2008;79:455–65.
- [2] Liljas M, Johansson P, Liu H-P, Olsson COA. Steel Res Int 2008;79:466–73.
- [3] Wang J, Uggowitzer PJ, Magdowski R, Speidel MO. Scripta Mater 1999;40:123–9.
- [4] Wessman SM, Hertzman S, Pettersson R, Lagneborg R, Liljas M. Mater Sci Technol 2008;24:348–55.
- [5] Herrera C, Ponge D, Raabe D. Steel Res Int 2008;79:482–8.
- [6] Pehlke RD, Elliot JF. Trans Metall Soc AIME 1960;218:1088–101.
- [7] Pickering FB. High nitrogen steels. In: Foct J, Hendry A, editors. Proceedings of the international conference organised by the institute of metals and the société française de métallurgie and held at Lille in France on May 18–20, 1988. London: Institute of Metals; 1989. p. 10–30.
- [8] Werner E. Mater Sci Eng A 1988;101:93–8.
- [9] Raabe D. Mater Sci Eng A 1995;197:31–7.
- [10] Raabe D. Mater Sci Technol 1995;11:455–60.
- [11] Humphreys FJ, Hatherly M. Recrystallization and related annealing phenomena. 2nd ed. Oxford: Elsevier; 2004. p. 628.
- [12] Lecroisey F, Pineau A. Metall Trans 1972;3A:387.
- [13] Rosen A, Jago R, Kjer T. J Mater Sci 1972;7:870–6.
- [14] Abbasi A, Dick A, Hickel T, Neugebauer J. Acta Mater 2011, in press.
- [15] Hickel T, Dick A, Grabowski B, Körmann F, Neugebauer J. Steel Res Int 2009;80:4–8.
- [16] Jun J-H, Choi C-S. Mater Sci Eng A 1998;257:353–6.
- [17] Foct J, Akdut N, Gottstein G. Scripta Metall Mater 1992;27:1033–8.
- [18] Akdut N, Foct J, Gottstein G. Steel Res 1996;67:450–5.
- [19] Olson GB, Cohen M. Metall Trans 1975;6A(4):791–5.
- [20] Murr LE, Staudhammer KP, Hecker SS. Metall Mater Trans A 1982;13(4):627–35.
- [21] Olson GB, Cohen M. J Less Common Metals 1972;28(1):107–18.
- [22] Mangonon PL, Thomas G. Metall Trans 1970;1(6):1577–86.
- [23] Verbeke K, Van Caenegem N, Raabe D. Micron 2009;40:151–6.
- [24] Schramm RE, Reed RP. Metall Mater Trans A 1975;6(7):1345–51.
- [25] Rhodes CG, Thompson AW. Metall Trans A 1977;8(12):1901–6.
- [26] Pozuelo M, Wittig JE, Jimenez JA, Frommeyer G. Metall Mater Trans A 2009;A40:1826–34.
- [27] Talonen J, Hänninen H. Acta Mater 2007;55:6108–18.
- [28] Reick W, Polhl M, Padilha AF. Steel Res Int 1996;67:253–6.
- [29] Humphreys FJ, Bate PS, Hurley PJ. J Microsc 2001;201:50–8.
- [30] Mesplont C, De Cooman BC. Mater Sci Technol 2003;19:875–86.
- [31] Zaefferer S, Ohlert J, Bleck W. Acta Mater 2004;52:2765–78.
- [32] Schulson EM. J Mater Sci 1977;12:1071–87.

- [33] Wilkinson AJ, Hirsch PB. *Micron* 1997;28:279–308.
- [34] Crimp MA. *Microsc Res Technol* 2006;69:374–81.
- [35] Zhai T, Martin JW, Briggs GAD, Wilkinson AJ. *Acta Mater* 1996;44:3477–88.
- [36] Ng BC, Simkin BA, Crimp MA. *Ultramicroscopy* 1998;75:137–45.
- [37] Gutierrez-Urrutia I, Zaefferer S, Raabe D. *Scripta Mater* 2009;61:737–40.
- [38] Gutierrez-Urrutia I, Zaefferer S, Raabe D. *Mater Sci Eng A* 2010;527:3552–60.
- [39] Raabe D. *Acta Mater* 1997;45:1137–51.
- [40] Raabe D, Ylitalo M. *Metall Mater Trans A* 1996;27:49–57.
- [41] Raabe D, Lücke K. *Scripta Metall* 1992;27:1533–8.
- [42] Raabe D, Lücke K. *Mater Sci Technol* 1993;9:302–12.
- [43] Hölscher M, Raabe D, Lücke K. *Steel Res* 1991;62:567–75.
- [44] Raabe D, Zhao Z, Park S-J, Roters F. *Acta Mater* 2002;50:421–40.
- [45] Wittig JE, Pozuelo M, Jimenez JA, Frommeyer G. *Steel Res Int* 2009;80:66–70.
- [46] Talonen J, Nenonen P, Pape G, Hänninen H. *Metall Mater Trans A* 2005;36:421–32.
- [47] Jacques PJ. *Curr Opin Solid State Mater Sci* 2004;8:259–65.
- [48] Stringfellow RG, Parks DM, Olson GB. *Acta Metall* 1992;40:1703–16.
- [49] Lee T-H, Oh C-S, Kim S-J. *Scripta Mater* 2008;58:110–3.
- [50] Angel T. *J Iron Steel Inst* 1954;177:165–74.
- [51] Sjöberg J. *Wire* 1973;23:155–67.
- [52] Nohara K, Ono Y, Ohashi N. *J Iron Steel Inst Jpn* 1977;63:212–22.

# Characterization of the Microstructure, Crystallographic Texture and Segregation of an As-cast Duplex Stainless Steel Slab

Clara Herrera, Dirk Ponge, Dierk Raabe

Max-Planck-Institut für Eisenforschung GmbH, Max-Planck-Str. 1, 40237 Düsseldorf, Germany; d.ponge@mpie.de

The microstructure of a duplex stainless steel slab 1.4362 produced by continuous casting has been investigated by optical microscopy, scanning electron microscopy, EBSD and EDS. The slab showed different macrostructures through the thickness. The macrostructure can be divided into 3 types: fine equiaxed, columnar and coarse equiaxed grains. In all three regions, the volume fraction of each phase austenite and delta-ferrite is close to 50% and the hardness is very similar for both. The austenite has Kurdjumov-Sachs or Nishiyama-Wassermann relationship with the delta-ferrite. The slab does not show a strong segregation profile through the thickness. The delta-ferrite is enriched in Cr and Mo, while austenite is enriched in Ni and Mn.

**Keywords:** duplex stainless steel, as-cast slab, microstructure, texture, EBSD, segregation

DOI: 10.2374/SRI08SP014-79-2008-482; submitted on 10 December 2007, accepted on 20 February

## Introduction

Duplex stainless steels (DSSs) are based on the Fe-Cr-Ni system and consist of ferrite (30-70%) and austenite. DSSs have shown an excellent combination of resistance to general and localized corrosion, stress corrosion cracking, high strength and low cost due to reduced contents of Ni and Mo [1-3]. DSSs are used in oil, gas, paper, desalination and petrochemical industries.

The main process steps in the industrial manufacturing of duplex stainless steel sheets are continuous casting, slab reheating, hot rolling, coiling, hot band heat treatment, cold rolling and final recrystallization annealing. Particular attention during manufacturing of these steels has to be paid to the forming steps at high temperatures. Hot working of steels with two phases may cause complications for several reasons: the precipitation of detrimental phases [1,4], such as  $\sigma$ -phase and  $M_{23}C_6$ , the low hot ductility, and edge crack formation. The ductility depends on different factors like temperature, strain rate, microstructure and chemical composition. Moreover, it is affected by the different softening mechanisms in ferrite and austenite [5-9].

The formation of as-cast microstructures of duplex stainless steels depends on undercooling, cooling rates and subsequent solid state transformations which are influenced by the local chemical composition [1,10-12]. Duplex stainless steels solidify by forming primary ferrite with austenite precipitates either from the liquid or in the solid state during cooling. The amount of austenite and its morphology depend on the cooling rate. At increased cooling rate the amount of austenite is reduced [10-14].

The austenite can have a specific orientation relationship with the ferrite matrix. Grains that have been formed by a  $\alpha$ - $\gamma$  phase transformation should show a Bain, Nishiyama-Wassermann (N-W), or Kurdjumov-Sachs (K-S) orientation relationship. These orientation relationships can be described as a rotation of an angle  $\omega$  about a common crystallographic axis (axis of rotation), this angle and axis are known as angle/axis pair, **Table 1**.

Owing to these aspects associated with the microstructural state of the two phases prior to hot working the present study investigates in detail the microstructure, the crystallographic microtexture, and the segregation of an as-cast duplex stainless steel slab produced by continuous casting (duplex stainless steel 1.4362).

**Table 1.** Orientation relationship between austenite ( $\gamma$ ) and ferrite matrix ( $\alpha$ ).

Orientation relationship	Lattice correspondence relation	Misorientation angle/axis
Bain	$\{001\}\gamma // \{001\}\alpha$ $\langle 110 \rangle\gamma // \langle 110 \rangle\alpha$	$45^\circ / \langle 001 \rangle$
Kurdjumov-Sachs (K-S)	$\{111\}\gamma // \{011\}\alpha$ $\langle 011 \rangle\gamma // \langle 111 \rangle\alpha$	$42.8^\circ / \langle 2\ 2\ 1 \rangle$
Nishiyama-Wassermann (N-W)	$\{111\}\gamma // \{011\}\alpha$ $\langle 112 \rangle\gamma // \langle 011 \rangle\alpha$	$45.9^\circ / \langle 254 \rangle$

**Table 2.** Chemical composition of the 1.4362 duplex stainless steel (mass %).

C	Si	Mn	Cr	Mo	Ni	Ti	Nb	Cu
0.024	0.220	1.39	22.32	0.14	3.65	0.012	0.010	0.410

## Experimental

The duplex stainless steel slab of 240mm thickness was produced by continuous casting under standard industrial condition. The chemical composition of the slab is given in **Table 2**.

Microstructural observations, optical and scanning electron microscopy (SEM) were performed on the plane normal to the transverse direction after standard sample preparation and etching using the solutions Beraha I [15] or V2A-etchant [16]. The volume fraction of the phases was quantified by optical microscopy and ferritoscope measurement (Helmut Fischer GmbH, model Ferritoscope

MP30E). No significant differences between the obtained values from both methods were found in this study.

A chemical analysis was performed by an energy dispersion spectroscopy (EDS) device attached to the SEM. Orientation imaging microscopy of the microstructure by automated EBSD measurements was applied. The step size for the measurements was between 1 and 10  $\mu\text{m}$ . Microhardness measurements were conducted using a load of 0.5 N.

## Results and Discussion

**Figure 1** shows the solidification macrostructure of the slab. The macrostructure of the slab consists of three zones: (a) a fine equiaxed zone at the top and bottom (Regions 1 and 4), (b) a columnar zone under the fine equiaxed zone on the top (Region 2), and (c) the equiaxed zone in the centre of the slab (Region 3). The macrostructure through the thickness of the slab is heterogeneous.

**Figure 2** shows a calculated portion of the phase diagram of the duplex stainless steel. After solidification and slow cooling, a coarse two-phase structure is observed. The as-cast microstructure is characterized by a ferrite matrix with austenite precipitates on the grain boundaries or inside the grains. **Figure 3 to 5** show the microstructure and **Table 3** the volume fraction of ferrite in the different zones of the slab. The slab does not reveal a strong gradient of the volume fraction of the two phases through the thickness. The ferrite solidifies first. The austenite precipitates in the solid state. The precipitation of austenite occurs by a nucleation and growth process. The austenite morphology can be characterized by Dubé [17] and Aaronson's [18] morphological classification scheme.

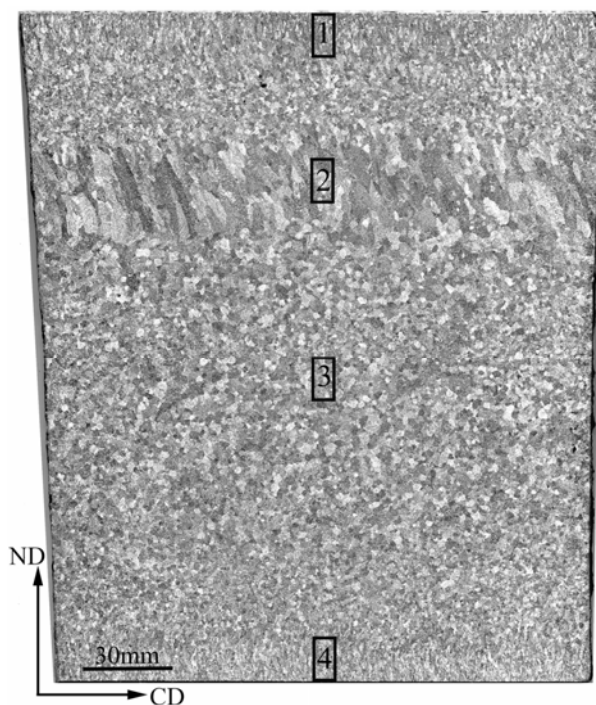


**Figure 1.** Macrostructure of duplex stainless steel 1.4362.

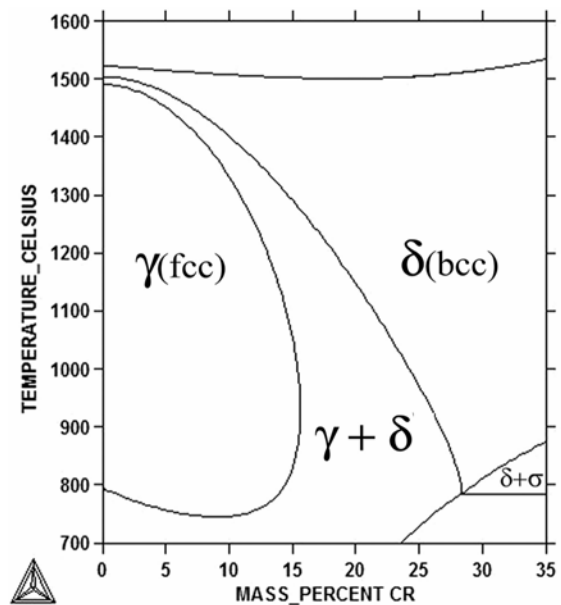


**Figure 2.** Cross-section of calculated phase diagram of Fe-Cr-3%Ni-0.14%Mo-1.4%Mn alloy.

**Table 3.** Volume fraction of ferrite in the different regions of the slab (cf. Figure 1).

Region	% Ferrite
1	49.3 ± 3.4
2	52.1 ± 3.9
3	56.2 ± 4.5
4	48.1 ± 3.9

**Table 4.** Hardness of austenite and ferrite in the four regions.

Region	Hardness, HV	
	Austenite	Ferrite
1	284.4 ± 11.6	284.8 ± 11.8
2	270.8 ± 13.8	280.8 ± 11.4
3	275.1 ± 17.2	255.3 ± 6.7
4	291.1 ± 13.9	281.7 ± 10.5

The austenite shows grain boundary allotriomorphs, Widmanstätten needles, or continuous films morphologies, respectively.

In the fine equiaxed zones (regions 1 and 4), the solidification is faster than in the other zones; therefore, the microstructure is finer. Austenite allotriomorphs are formed first at the ferrite grain boundaries. Starting from them Widmanstätten austenite needles extend inside the ferrite grains. Large arrays of parallel austenite needles are observed.

Region 2 exhibits columnar ferrite grains with continuous austenite films on the grain boundaries. Long austenite needles or bigger allotriomorphs can also be detected.

In the centre of the slab, region 3, the ferrite shows equiaxial grains which are larger than the ferritic grains at the top and bottom of it due to the slow cooling rate.

The hardness of the austenite and ferrite do not change substantially through the thickness (**Table 4**). The hardness

values are common duplex stainless steels [19-21]. The ferrite in the middle of the slab shows a low hardness due to the coarse grain size in this region.

The slab does not show substantial segregation through the thickness. The concentration of Cr, Ni, Mn and Mo in the austenite and ferrite are very similar in the four regions. **Figure 6** shows the distribution of Fe, Cr, Ni, Mn in both phases as a function of the partition coefficient  $K_p$ .

Distribution maps of Cr, Ni, Mn, Si and Mo were collected together with the corresponding EBSD scans (**Figure 7c** and **7d**). The EBSD technique is sensitive to different lattice parameters as well as to crystallographic orientations.

In the regions 1 and 4, the distribution of the elements is homogeneous. In regions 2 and 3, Mn and Si show a homogeneous distribution in both phases while ferrite is Cr-enriched and austenite is Ni-enriched. This elemental partitioning corresponds to the stabilizing effect of each element [22-25]. The distribution of Mo is homogeneous between both phases in regions 1, 3 and 4 but it is not detectable in region 2 because the concentration of Mo is too low for a quantitative measurement by EDS. Ohmori et al. [22] reported that the partition of Mo between austenite and ferrite was very minor compared with Ni and Cr partitions.

The decomposition of  $\delta$ -ferrite can take place by the nucleation and growth process with partitioning of Ni and Cr atoms between the austenite and the ferrite [26]. The partition must occur at the ferrite-austenite grain boundary

during cooling. The variation of the elemental distribution in the different regions is related to the cooling rate. It is fastest in regions 1 and 4. Consequently, the time for diffusion processes is shorter compared with the other zones. In the regions 2 and 3, the slow cooling favours the diffusion of the elements.

The texture of the slab is not strong but it shows a gradient through the thickness. **Figure 8** shows pole figures for austenite and ferrite determined by EBSD. In region 2, the ferrite texture is strongest. Regions 1 and 4 show the weakest texture. The ferrite texture in regions 2 and 3 is more pronounced due to the slower cooling rate. The austenite texture shows a weak intensity in all regions compared with the ferrite texture. The ferrite texture develops during the solidification process, while the austenite texture results from the  $\delta \rightarrow \gamma$  transformation.

In regions 1 and 4, the ferrite grains forms  $\{001\}\langle 110 \rangle$  and  $\{012\}\langle 321 \rangle$  components. The austenite phase shows a strong component close to  $\{110\}\langle 332 \rangle$  and a weak  $\{001\}\langle 021 \rangle$  component. In region 2, the texture of the ferrite is characterized by  $\{001\}\langle 210 \rangle$  and  $\{112\}\langle 021 \rangle$  and the austenite by  $\{110\}\langle 113 \rangle$  and  $\{001\}\langle 120 \rangle$  texture components. The ferrite texture is tilted, approximately  $10^\circ$ , in relation to the normal direction due to the thermal gradient. In region 3, the ferrite shows a texture fibre  $\langle 001 \rangle // ND$  and austenite shows  $\{110\}\langle 113 \rangle$  and  $\{032\}\langle 123 \rangle$  components.

During continuous casting, the top and bottom of the slab solidified at first with a high cooling rate. The ferrite

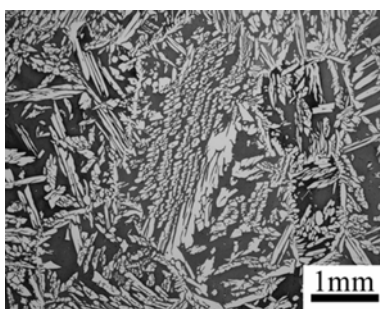
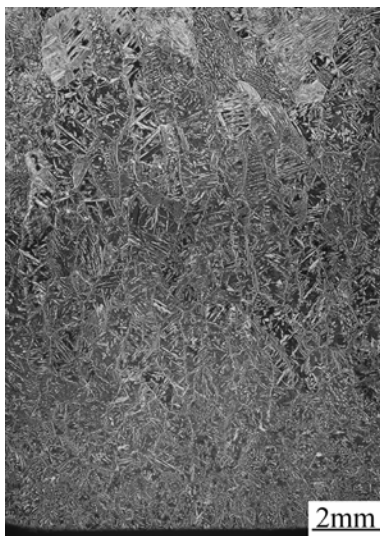


**Figure 3.** Microstructure at the top and the bottom of the slab, region 1.

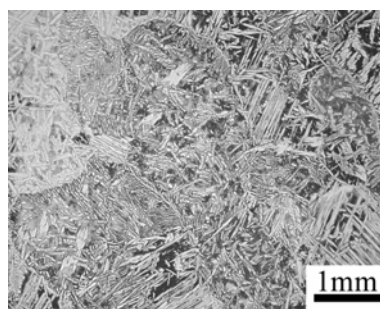


**Figure 4.** Microstructure of the columnar zone, region 2.

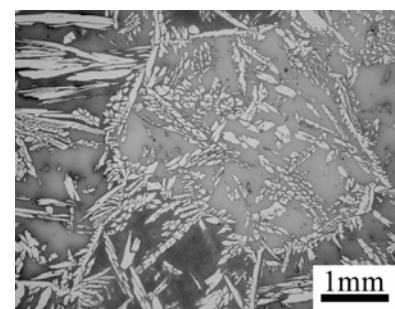
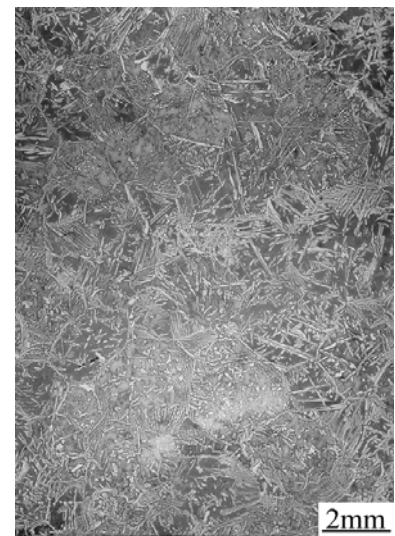


**Figure 5.** Microstructure at the middle of the slab, region 3.

texture in these regions is almost random due to the heterogeneous nucleation at the interface between the mould walls and the liquid metal in the solidification, as known from other conventional casting processes. In region 2, the columnar ferrite grains are elongated in the direction of the heat flow, and have a strong crystallographic texture. In region 3, equiaxed grains are formed with a more random texture compared with the columnar region [27].

A favourable orientation in the solidification process occurs when the direction of growth is perpendicular to the mould wall, for cubic metals, the preferred growth direction is  $\langle 001 \rangle$ , which results in the gradual strengthening of the  $\langle 001 \rangle$ //ND fibre texture. The ferrite texture of the slab is a typical texture observed in the solidification of cubic metals. The solidification texture of the ferrite is in principal comparable to earlier observations on single phase  $\alpha$ - and  $\gamma$ - stainless steels [28-30].

Figures 7a and 7b show a phase map with the orientation relationships between  $\delta$  and  $\gamma$  obtained by EBSD measurements of one of the samples, region 2. Figure 9 shows the distribution of the misorientation angle between  $\delta$  and  $\gamma$  boundaries. The used tolerances for the orientation relationship are  $2.5^\circ$  or  $5^\circ$  around the misorientation angle. The misorientation of the three regions lies in the interval of  $40$ - $50^\circ$ , which contains both the Nishiyama-Wassermann (N-W) and the Kurdjumov-Sachs (K-S) crystallographic orientation relationships. The Bain orientation relationship is not observed in any of the three regions. The misorientation angle distribution for this interval reveals a maximum around  $44^\circ \pm 2^\circ$ . The phase map (Figure 7b) shows that the austenite precipitates with a near N-W or K-S orientation relationship with at least

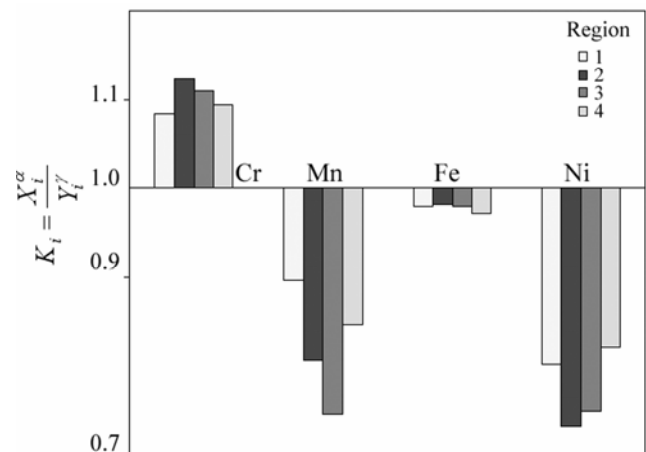


Figure 6. Partition coefficient of the alloying elements in the three regions.

one grain. This result agrees with earlier results from the literature [31,32]. The distribution of the orientation relationships shows that the K-S orientation relationship occurs more frequently than the N-W orientation relationship. It also shows that the variant 1 of the K-S orientation relationship [33],  $(111)\gamma // (011)\alpha - [101]\gamma // [\bar{1}\bar{1}1]\alpha$ , is the most frequent one. This behaviour was found in all three regions. Most of the Widmanstätten needles and allotriomorphs of the austenite grow with a specific orientation relationship with the ferrite and do so close to K-S or N-W relationships.

The austenite regions, which grow by a reconstructive mechanism into the ferrite grains, tend to grow without a strict crystallographic orientation relationship into only one

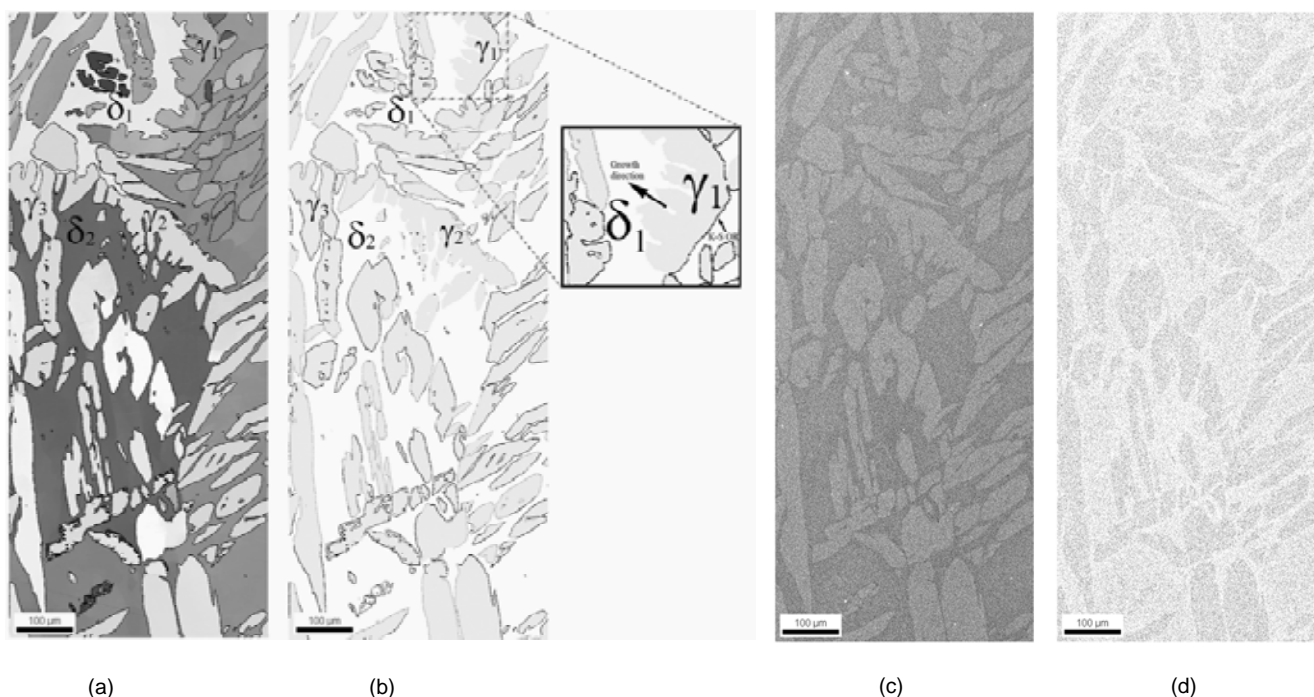


Figure 7. EBSD orientation map of the region 2: (a) IPF map showing the orientation of the two phases; (b) grain average misorientation map between  $\delta$  ferrite (white) and austenite (grey); (c) EDS map of Cr distribution and (d) EDS map of Ni distribution.

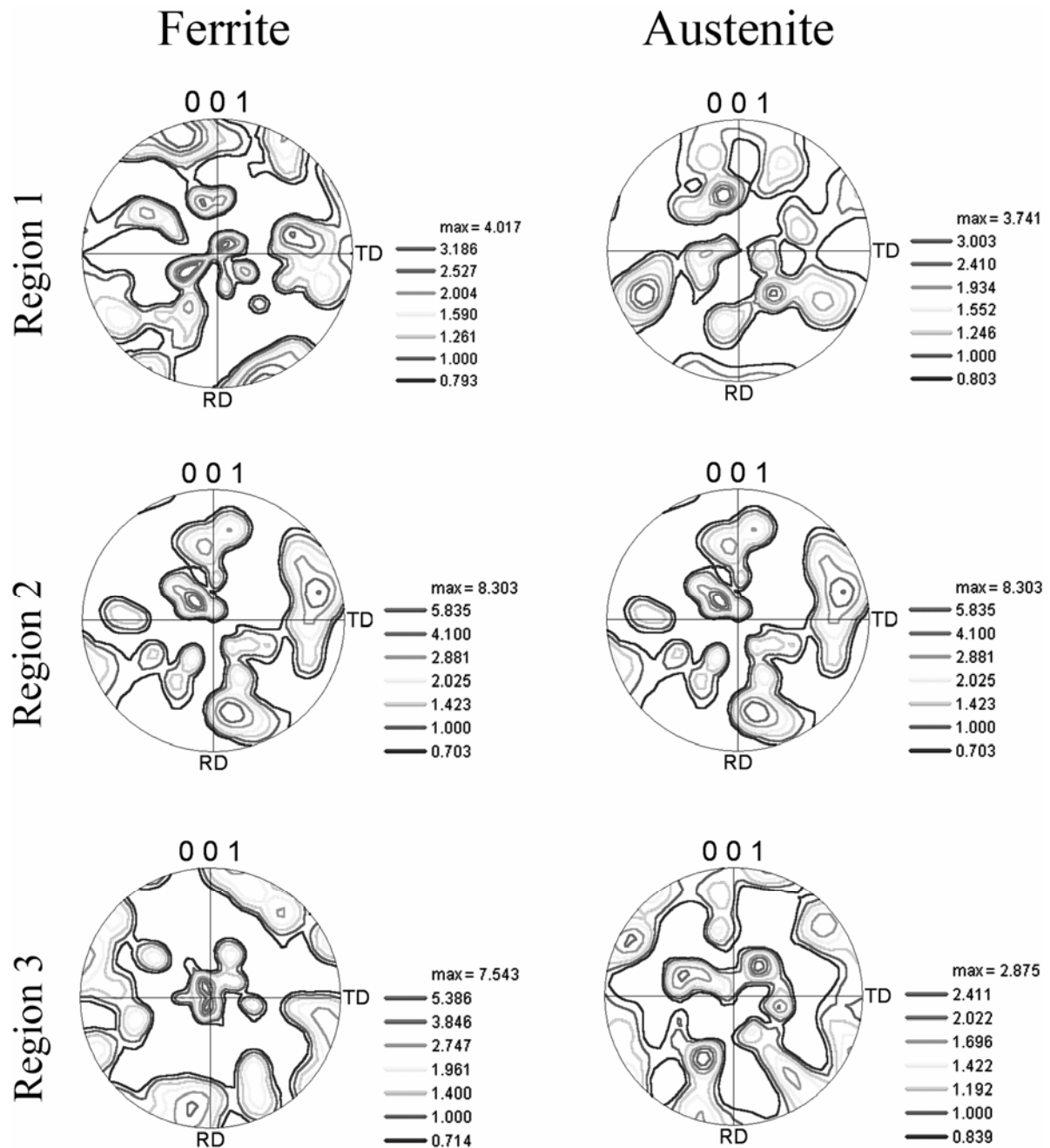


Figure 8. {001} Pole figures of austenite and  $\delta$  ferrite of the three regions.

$\delta$ -ferrite grain. The other side of the  $\gamma$  grain, which nucleates with a low-energy grain boundary, does not move and has a preferred orientation relationship [31,32,34,35]. Austenitic grains, which are identified as  $\gamma_1$  and  $\gamma_2$ , grow into  $\delta_1$  and  $\delta_2$ , respectively, this behaviour is shown in **Figure 7b**. In some cases, austenite grows into both  $\delta$  grains with a specific orientation relationship, e.g.  $\gamma_3$  grows into  $\delta_1$  and  $\delta_2$  (**Figure 7b**).

The  $\delta$ -ferrite solidifies preferentially in the [100] direction and the austenite precipitates holding a specific relationship with their ferrite matrix. Davies et al. [36] observed that the phase transformation in a commercial duplex  $\alpha$  -  $\beta$  brass (59.5%Cu-40.5%Zn) is also orientation dependent. The measurement of the  $\alpha$ -brass texture that these authors conducted in their work was characterized by

a cube texture,  $\{001\}\langle 100\rangle$ , a texture fibre running from the  $\{110\}\langle 112\rangle$  to the near  $\{112\}\langle 111\rangle$  orientation, and a further fibre texture between  $\{103\}\langle 010\rangle$  and  $\{101\}\langle 010\rangle$ . This texture is similar to the texture that would be predicted using the K-S relationship between  $\beta$ - and  $\alpha$ -brass.

The  $\alpha$ -brass textures from this earlier work and the  $\gamma$  textures observed in the current study are comparable. Therefore, it is concluded that the  $\delta$ - $\gamma$  transformation can be described by the K-S or N-W type relationships. Finally, when the cooling of the continuous casting is slow, the transformation takes place close to thermal equilibrium and any crystallographic relationship in a diffusive solid-state transformation can develop more accurate [37].

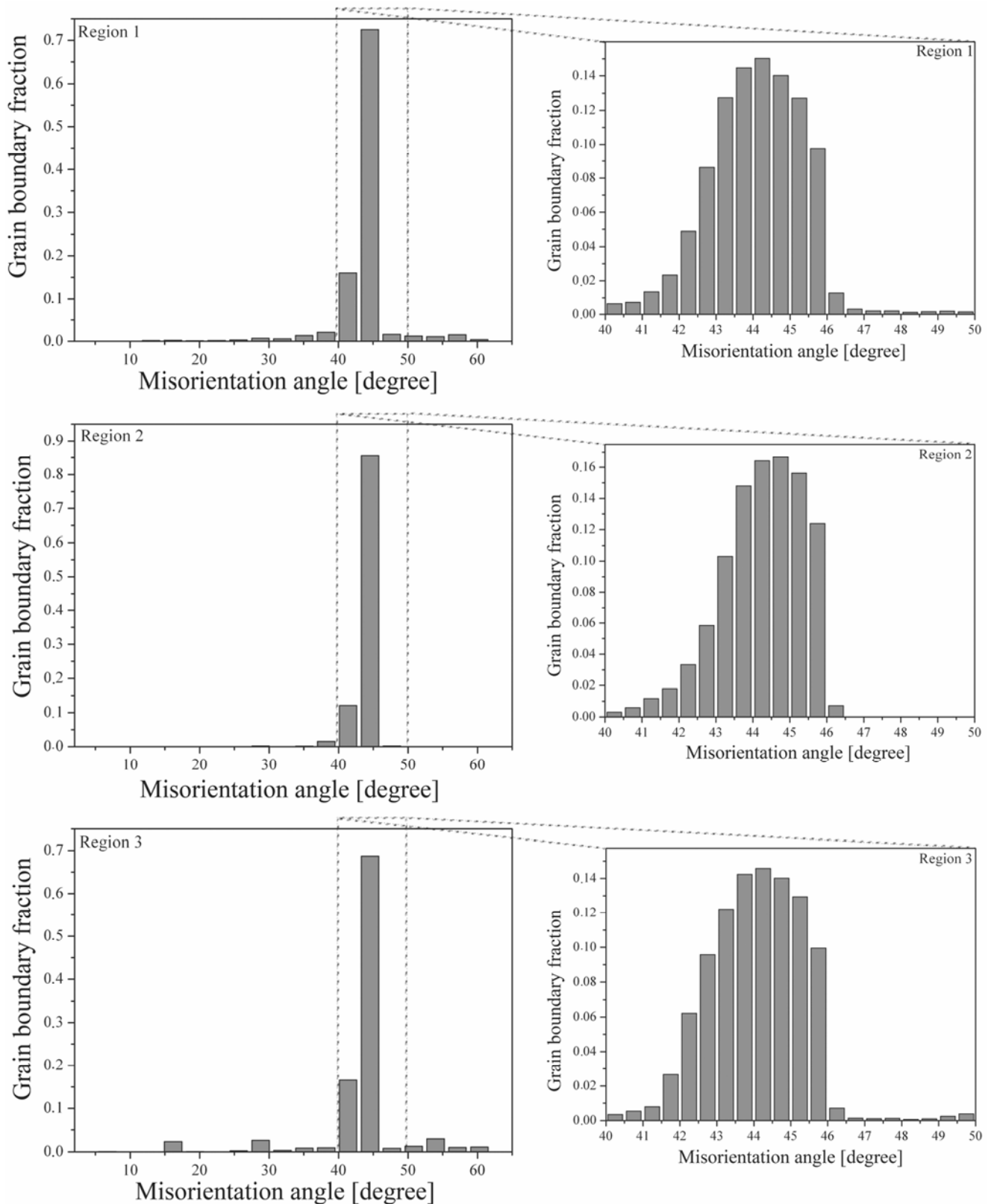


Figure 9. Histograms of misorientation angle distribution between  $\delta$  ferrite and austenite of the three regions.

## Conclusions

The duplex stainless steel slab produced by continuous casting showed a ferritic-austenitic microstructure. The austenite precipitated at the grain boundaries or inside

the  $\delta$ -ferrite with Nishiyama-Wassermann (N-W), or Kurdjumov-Sachs (K-S) orientation relationship to the ferrite. The phase fractions were constant through the thickness. After solidification, an equal volume fraction of ferrite and austenite, close to 50-50%, was obtained for the

temperature range between 1200 to 1100°C. The cooling rate from this temperature range to room temperature was similar everywhere in the slab. Consequently, the volume fraction of the phases did not show a significant variation through the thickness. The austenite morphology can be described by Dubé and Aaronson's morphological classification. The slab shows a finer microstructure at the top and bottom, a small columnar region close to the top and a coarse equiaxed microstructure in the middle. The ferrite texture is a typical solidification texture, dominated by <100>ND, and it is strongest in the columnar region. The austenite texture is weaker. The element partitioning between  $\delta$  ferrite and austenite is stronger in the columnar and equiaxed regions near the centre of the slab due to the slower cooling rate favouring diffusion. In these regions, austenite is enriched in Ni and Mn while  $\delta$  ferrite has more Cr and Mo.

References

[1] J.-O. Nilsson: *Materials Science Technology*, 8 (1992), No. 8, 685-700.

[2] H.D. Solomon, T.M. Devine: *Duplex Stainless Steel - A tale of two phase*, Conference Duplex Stainless Steel'82, 1982 St. Louis, USA, Proceedings. Metals Park, Ohio, ASM, 1983, p.693-756.

[3] D. Noble: *Selection of wrought duplex stainless steel*, ASM Handbook, Metals Park, Ohio; ASM International, 6 (1993), p.471-781.

[4] A. Wilson, J.-O. Nilsson: *Scand. J. Metallurgy*, 25 (1996), No. 4, 178-185.

[5] E. Evangelista, H.J. McQueen, M. Niewczas, M. Cabibbo: *Canadian Metall. Quarterly*, 43 (2004), No. 3, 339-354.

[6] O. Balancin, W.A.M. Hoffmann, J.J. Jonas: *Metall. Mat. Trans. A*, 31 (2000), No. 5, 1353-1364.

[7] L. Duprez, B.C. De Cooman, N. Akdut: *Steel Research*, 73 (2002), No. 12, 531-538.

[8] A. Iza-Mendia, A. Pinol-Juez, J.J. Urcola, I. Gutierrez: *Metall. Mat. Trans. A*, 29 (1998), No. 12, 2975-2986.

[9] J.M. Cabrera, A. Mateo, L. Llanes, J.M. Prado, M. Anglada: *J. Materials Processing Technology*, 143-144 (2003), p. 321-325.

[10] Z.M. Cvijovic, D.V. Mihajlovic, V.R. Knezevic: *Materials Science Forum*, 282-283 (1998), 323-330.

[11] E. Gariboldi, N. Lecis, F. Bonollo, N. Gramegna, W Nicodemi: *Advanced Engineering Materials*, 4 (2002), No. 1-2, 33-37.

[12] C. Herrera, N.B. de Lima, A.M. Kliauga and A.F. Padilha: *Materials Characterization*, 59 (2008), No. 1, 79-83.

[13] E. Johnson, L. Gråbæk, A. Johansen, L. Sarholt Kristensen: *Materials Science Engineering*, 98 (1988), 301-303.

[14] S.A David, J.M. Vitek, T.L. Hebble: *Welding Research Sup.*, (1987), No. 10, p. 289S-300S.

[15] E. Weck, E. Leistner: *Metallographische Anleitung zum Farbätzen nach dem Tauchverfahren, Teil II*, Deutscher Verlag für Schweisstechnik, München, Germany, 1983.

[16] G. Petzow: *Metallographisches Ätzen*, Gebrüder Borntäger, Berlin, Germany, 1984.

[17] C. Dubé, H. Aaronson, R.F. Mehl: *Revue de Metallurgie*, 55 (1958), No. 3, 201-210.

[18] H. Aaronson, in: *Decomposition of austenite by diffusional processes*, ed. V. Zachay, H. Aaronson, Interscience Publishers, 1962, pp. 387-546.

[19] A. Ulhaq, H. Weiland, H.J. Bunge: *Materials Science and Technology*, 10 (1994), No. 4, 289-298.

[20] A.F. Padilha, V. Randle, I.F. Machado: *Materials Science and Technology*, 15 (1999), No.9, 1015-1018.

[21] M. Martins, L.C. Casteletti: *Materials Characterization*, 55 (2005), 225-233.

[22] Y. Ohmori, K. Nakai, H. Ohtsubo, Y. Isshiki. *ISIJ International*, 35 (1995), No. 8, 969-975.

[23] S. Atamert, J.E. King: *Acta Metall. Mat.*, 39 (1991), No.3, 273-285.

[24] T.H. Chen, J.R. Yang: *Materials Science Eng A*, 311 (2001), 28-41.

[25] J.M. Vitek, S.A. Vitek, S.A. David. *Metallurgical and Materials Transactions A*, 26 (1995), No. 8, 1995-2007.

[26] P.D. Southwick and R.W.K Honeycombe: *Metal Science*, 14 (1980), No. 7, 253-261.

[27] B. Chalmers: *Principles of solidification*, John Wiley & Sons, Inc., New York, 1967.

[28] D. Raabe: *Metallurgical Materials Transactions A*, 26 (1995), No. 4, 991-998.

[29] D. Raabe: *Materials Science and Technology*, 11 (1995), No. 5, 461-468.

[30] D. Raabe: *Acta Materialia*, 45 (1997), No. 3, 1137-1151

[31] K. Ameyama, G.C. Weatherly, K.T. Aust: *Acta Metall. Mater.*, 40 (1992), No. 8, 1835-1846.

[32] E.F. Monlevade, I.G.S. Falleiros: *Metallurgical Materials Transaction A*, 37 (2006), No. 3, 939-949.

[33] S. Morito, H. Tanaka, R. Konishi, T. Furuhashi, T. Maki: *Acta Materialia*, 51 (2003), 1789-1799.

[34] C.H. Shek, C. Dong, J.K.L. Lai, K.W. Wong: *Metallurgical Materials Transactions A*, 31 (2000), No. 1, 15-19.

[35] H. Landheer, S.E. Offerman, R.H. Petrov, L.A.I Kestens, *Materials Science Forum*, 558-559 (2007), 1413-1418.

[36] G.J. Davies, J.S. Kallend, P.P. Morris: *Acta Metallurgical*, 24 (1976), 159-172.

[37] H.J. Bunge, W. Weiss, H. Klein, L. Weislak, U. Garbed, J. R. Schneider: *J. Applied Crystallography*, 36 (2003), 137-140.